

1 **Geochemical and granulometric fingerprints of 8,200-year**
2 **Westerly variability recorded in an inner-fjord lake sediments**
3 **from Central Svalbard**

4 Zofia Stachowska ^{1*}, Willem G. M. van der Bilt ², Jan Kavan ³, Mark F. A. Furze ⁴, Ingunn H.
5 Thorseth ⁵ and Mateusz C. Strzelecki ⁶

6

7 ^{1*} *zofia.stachowska@usz.edu.pl, Institute of Marine and Environmental Sciences, Doctoral*
8 *School, University of Szczecin, ul. Mickiewicza 16, 70-383 Szczecin, Poland*

9 ² *willemvanderbilt@uib.no, Department of Earth Science and Bjerknes Centre for Climate*
10 *Research, University of Bergen, Allégaten 41, 5007 Bergen, Norway*

11 ³ *jan.kavan.cb@gmail.com, Centre for Polar Ecology, Faculty of Science, University of South*
12 *Bohemia, Na Zlaté stoce 3, 370 05 České Budějovice, Czechia*

13 ⁴ *markf@unis.no, Department of Arctic Geology, The University Centre in Svalbard, P.O.*
14 *Box 156 N-9171, Longyearbyen, Norway*

15 ⁵ *ingunn.thorseth@uib.no, Centre for Deep Sea Research, Department of Earth Science,*
16 *University of Bergen, Allégaten 41, 5007 Bergen, Norway*

17 ⁶ *mateusz.strzelecki@uwr.edu.pl, Alfred Jahn Cold Regions Research Centre, Institute of*
18 *Geography and Regional Development, University of Wrocław, ul. Fryderyka Joliot-Curie 12,*
19 *50-383 Wrocław, Poland*

20

21 This paper is a non-peer-reviewed preprint submitted to EarthArXiv. This original paper was
22 submitted to *Boreas* for peer review on April 3, 2026.

23

24

25 **Abstract**

26

27 The Arctic is warming faster than any other region on Earth. As sea-ice diminishes, surface
28 boundary conditions (roughness and air-sea coupling) change and open-water fetch increases,
29 potentially strengthening the effective wind forcing on Arctic coasts. These changes can be
30 recorded in lake sediments through the deposition of wind-blown grains and elements, offering
31 insights into past wind and climate dynamics. We reconstruct ca. 8,200 yrs of wind-climate
32 variability using laminated sediments from a closed-basin lake in the Central part of the High
33 Arctic Svalbard archipelago. By integrating geochemical, visual, and granulometric
34 fingerprints within a multiproxy geostatistical framework, we link wind-blown minerogenic
35 input to specific catchment sources and show that iron (Fe)- and titanium (Ti)- enriched clasts
36 originate from distinct dolerite outcrops West of the lake, upwind of the dominant summer
37 Westerlies. These results reveal a locally filtered Westerly input, consistent with valley-fjord
38 channelling. We identify four Mid- and Late Holocene phases of enhanced eolian activity that
39 occurred during intervals when local boundary conditions favoured the entrainment and
40 transport of sediment into the basin. Unit-scale sedimentation shifts can be placed at the end of
41 the Holocene optimum and at the stepwise onset of the Neoglacial. However, the reconstructed
42 wind signal shows comparatively stable long-term behaviour and no direct correspondence with
43 paleoclimate records.

44

45 *Keywords: Westerly winds, Lake sediments, Spitsbergen, Holocene, Sediment provenance, End*
46 *Member Modelling*

47 **1. Introduction**

48
49 The Arctic is warming at nearly four times the global average – a phenomenon known as Arctic
50 amplification (Rantanen et al., 2022). This rapid warming leads to cryosphere degradation,
51 which enhances the supply of unconsolidated material available for eolian transport. Yet the
52 geomorphic response to a warmer Arctic is unlikely to be monotonic, because sea-ice not only
53 limits fetch and coastal exposure, but also mediates momentum transfer and effective surface
54 forcing (Mulwijk et al., 2024). While wind is a primary driver of Arctic geomorphic change,
55 instrumental observations provide only a brief baseline for High Arctic wind variability
56 (Rasmussen et al., 2023; Rymer et al., 2022; St. Louis et al., 2024). Paleoenvironmental
57 archives are therefore essential for extending these time series and testing how eolian erosion
58 thresholds and depositional filtering of eolian input vary across different climate states
59 (Kylander et al., 2023; Stachowska et al., 2024). Lacustrine sediments are particularly valuable,
60 as they trap wind-blown mineral particles preserved as changes in minerogenic flux, density,
61 and grain size (Hess et al., 2023; Saunders et al., 2018; Stachowska et al., 2024). In settings
62 with contrasting catchment sources, this signal can be isolated by combining high-resolution
63 core scanning with granulometric unmixing and source validation (Stachowska et al., 2024).
64 Here, we apply that workflow to identify provenance-specific eolian input in a topographically
65 complex Arctic setting.

66
67 We investigate Dunsappietjørna, a lake in Gipsdalen, a valley in Central Spitsbergen
68 (Svalbard). This study area lies within the climatic boundary between the North Atlantic and
69 the Arctic Ocean (Farnsworth et al., 2020), and the archipelago is recognised as an Arctic
70 climate-change hotspot, having warmed by $\sim 4^{\circ}\text{C}$ over the past century (Førland et al., 2011;
71 Nordli et al., 2020). Postglacial isostatic uplift here generally exceeds global sea-level rise,

72 resulting in continuous Holocene sedimentary archives (Salvigsen, 1984; Stachowska et al.,
73 2024; Strzelecki et al., 2026). We target a lake in this inner fjord-valley system to test how local
74 topography, sea-ice-modulated exposure, and sediment availability shape the translation of
75 atmospheric variability into a depositional signal. Modern observations from Isfjorden show
76 pronounced spatial heterogeneity in near-surface wind direction and speed, driven by valley-
77 fjord geometry, land-sea contrasts, and air-sea-ice interactions, making this setting suitable for
78 evaluating local filtering of a broader wind signal (Frank et al., 2023a, 2025). Our study area
79 also contains seasonally reworked sediments derived from contrasting sedimentary and igneous
80 lithologies (Dallmann, 2015; NPI Geological maps, 2026), offering a foundation for examining
81 how atmospheric regimes manifest in sheltered, topographically complex locations.

82

83 This study presents a ca. 8,200-year-long archive of summer Westerly winds reconstructed from
84 Dunsappietjørna sediments (Fig. 1B). By applying a multiproxy approach, we link downcore
85 changes in eolian clastic input to Fe-Ti-rich grains derived from local dolerite outcrops West of
86 the lake (Dallmann, 2015; NPI Geological maps, 2026; Senger et al., 2014), providing a
87 diagnostic provenance target for wind-blown minerogenic input. We distinguish the eolian
88 component from other parallel depositional processes and test whether the record expresses
89 broader atmospheric forcings or a locally filtered signal imposed by inner-fjord-valley
90 geometry, sea-ice-modulated exposure (Frank et al., 2025), and changes in sediment availability
91 (Strzelecki et al., 2026). We then compare major transitions in the Dunsappietjørna record with
92 selected local and regional records of Holocene glacial activity (Farnsworth et al., 2020;
93 Forwick et al., 2010), sea-ice, ice rafting, and temperature (Kong et al., 2025; Müller et al.,
94 2012a, b; Rasmussen et al., 2012), and try to evaluate how these boundary conditions influence
95 sediment entrainment and depositional filtering in inner-fjord settings – an issue of increasing
96 importance as Arctic warming alters wind patterns and coastal exposure.

97

98 **2. Study area**

99

100 Gipsdalen, situated in Bünsow Land, on Central Spitsbergen, is ~25 km long and ~3 km wide
101 U-shaped valley (Fig. 1C). Several outlet glaciers head into the valley (e.g., Florabreen,
102 Margaretbreen, Methuenbreen, Boltonbreen, and Stenhousebreen), all located on the
103 surrounding plateau and in proximity to the Filchnerfonna (East) and Lomonosovfonna (North)
104 ice caps (Fig. 1C; Brekke and Hansson, 1990; Dallmann, 2015; Forwick et al., 2010). The
105 bedrock comprises Late Carboniferous to Early Permian sedimentary rocks from the
106 Billefjorden, Gipsdalen, and Tempelfjorden Groups (limestone, dolomite, gypsum, marl,
107 sandstone and coal-bearing shale; Brekke and Hansson, 1990; Dallmann, 2015). In contrast, the
108 Early Cretaceous dolerites of the Diabasodden Suite (Nejbert et al., 2011; NPI Geological maps,
109 2026; Senger et al., 2014), typically medium- to fine-grained and containing Fe and Ti oxides,
110 such as ilmenite and titanomagnetite (Nejbert et al., 2011; Senger et al., 2014), outcrop at
111 several localities in Eastern and Southeastern Isfjorden. Out of these, the largest, located closest
112 to the catchment, lie at Gisphukodden, a coastal promontory Northwest of the valley, as well as
113 on Gåsøyane, and at Kapp Thordsen, Northwest of Gipsvika (Fig. 1C), West of the catchment
114 (Brekke and Hansson, 1990; Nejbert et al., 2011; NPI Geological maps, 2026; Senger et al.,
115 2014).

116

117 Our study site, Dunsappietjørna (78°27'N, 16°41'E, ~65 m a.s.l.), is a small, shallow basin (0.06
118 km², ~3.3 m deep) located in Southeastern Gipsdalen, within a sparsely vegetated raised
119 shoreline complex on the coast of Gipsvika (Fig. 1C-E). Local relative sea-level (RSL) records
120 from inner Isfjorden document rapid Early Holocene postglacial emergence and continued RSL
121 fall. While the available curves do not permit a precise isolation age for a basin at ~65 m a.s.l.,

122 they do indicate that it occurred in the Early Holocene (Forman et al., 2004; Salvigsen, 1984;
123 Strzelecki et al., 2026). An independent emergence constraint from Petuniabukta (Billefjorden),
124 where a whale bone was found at 58.1 m a.s.l., and dated back to 10,300 cal. yrs B.P., suggests
125 that 65 m a.s.l. could correspond to ca. 10,700 cal. yrs B.P. (Lulák et al., 2026). Geomorphic
126 constraints for inner Isfjorden indicate a postglacial marine limit of at least ~72 m a.s.l. (Forman
127 et al., 2004; Salvigsen, 1984; Strzelecki et al., 2026). Following emergence, the lake's basin
128 likely formed within a shallow fjord embayment. As shown in Figs. 1D-E and S1A, it is
129 dammed by sandy-to-gravelly beach-ridges with inter-ridge marsh complexes containing
130 occasional silty layers. Clayey-silty marine deposits occur landward of the ridges, and
131 gelifluction material covers the valley sides. The Gipsdalselva system includes active alluvial
132 reaches and floodplains, including Leirflata – a floodplain located Northwest of the lake. A
133 sandy-gravelly alluvial fan borders the beach-ridge system to the Southwest. Numerous sand-
134 dominated eolian deposits are also present in this part of the valley, particularly North of the
135 Gipsdalselva mouth, around Leirflata, and farther into Gipsdalen (Figs. 1D-E and S1A; Brekke
136 and Hansson, 1990).

137
138 Data from 1991-2020 C.E. show that the mean annual air temperature at the Svalbard Lufthavn
139 weather station (~33 km Southwest) remained below freezing (around -4°C), with an average
140 annual precipitation of ~200 mm (MET Norway, 2026), which is consistent with the broader
141 climatic characterisation of Central Svalbard (Førland et al., 2011). The long-term observational
142 record (1981-2010) by Førland et al. (2011) further indicates an overall rise in al temperature
143 during recent decades. Sentinel-2 satellite imagery confirms that the lake and the area are
144 typically ice-free from July to September (Fig. S2; ESA, EC, 2023). During fieldwork in March
145 2024, the lake ice surface was not exposed, and the snow cover showed no obvious
146 accumulation of wind-blown sediment. No evidence of water-level drawdown or shoreline

147 displacement was noted during the field campaigns. However, our field observations and
148 remotely sensed data suggest that the Eastern side of the catchment may be affected by summer
149 meltwater discharge from Dalkallen and Aitkenfjellet, as evidenced by ephemeral streams
150 (Figs. 1D-E, and S1A-B). Wind observations from the Gåsøyane lighthouse station show that
151 the area is influenced by both Westerlies and Easterlies, revealing distinct seasonal patterns
152 (Fig. 1B and ‘Supplementary Note 1’). During winter (December-February; DJF), Northerly
153 and Northeasterly winds dominate, with weaker Easterly contributions, while Westerlies are
154 less frequent but have the highest mean speed, averaging 12.3 m/s (a strong breeze). In contrast,
155 summer (June-August; JJA) winds mainly come from the Southwest and Northwest directions
156 and average 5.3 m/s (a gentle breeze), while the Northerly and Northeasterly flow is less
157 frequent but stronger, averaging 7.0 m/s (a moderate breeze; Fig. 1B and ‘Supplementary Note
158 1’). However, Frank et al. (2023b) report that local topographic effects near the weather station
159 amplify measurements for these winds.

160

161 **3. Material and methods**

162 **3.1. Fieldwork**

163

164 A bathymetric survey of the lake was conducted during the field campaign in September 2023
165 using a Lowrance Elite-9 Ti² fish finder echosounder. We targeted a coring site in a flat central
166 section of Dunsappietjørna’s Northwest part, at a water depth of ~3.3 m (see Fig. 1D). Next,
167 we retrieved a ~121 cm-long sediment core DST-2023 GC, using a UWITEC gravity coring
168 system fitted with 9 cm diameter liners. Additionally, during a separate field campaign in July
169 2024, four catchment samples (CSs) were collected to aid source-to-sink analysis (Figs. 1E and
170 S1): one from an Easterly inlet to the lake (CS 1), two from a fluvial floodplain Northwest of
171 the lake (CS 2 and 4), and one from an alluvial fan Southwest of the lake (CS 3).

172

173 **3.2. Stratigraphy and geochemistry**

174

175 Following fieldwork, the core was split lengthwise at the EARTHLAB facility at the University
176 of Bergen (UiB) and stored at 4°C in between analyses. The core was then visually logged and
177 photographed using an optical (RGB) line camera. Next, we performed non-destructive
178 scanning analyses. To map minerogenic element input to Dunsappietjørna, we used an ITRAX
179 X-Ray Fluorescence (XRF) scanner at the EARTHLAB (UiB), equipped with a Chromium (Cr)
180 tube (Cox Analytical System, 2008), set to 40 kV and 10 mA, to detect lighter lithogenic
181 elements that characterise the carbonate-bearing catchment bedrock (Rothwell and Croudace,
182 2015). A total of 25 elements were analysed downcore at 200- μm intervals. Computed
183 Tomography (CT) scanning was subsequently performed to capture downcore variations in
184 density and visualise sediment structure in 3-D, using CT grayscale values (van der Bilt et al.,
185 2018b). Scanning was performed using a ProCon X-ray CT-ALPHA scanner at the
186 EARTHLAB facility (UiB), operated at 120 kV and 800 μA with a 267 ms exposure time, and
187 acquiring 2,400 images per rotation. To minimise the impact of beam hardening (Brooks and
188 Di Chiro, 1976), we applied a 1-mm copper (Cu) filter. Downcore CT grayscale variations were
189 mapped at 500 μm resolution using the SplineProbe tool in Thermo Fisher Avizo version 9.
190 Following non-destructive scanning, we extracted 121 samples for physical analyses at
191 contiguous 1 cm intervals using a 0.3 cm-wide syringe. Samples were dried for 12 hours at
192 105°C to determine Dry Bulk Density (DBD; g/cm^3), and combusted for four hours at 550°C
193 in a muffle furnace to determine organic content by means of Loss on Ignition (LOI, %; Dean,
194 1974; Heiri et al., 2001). Finally, the remaining sample residues, along with four catchment
195 samples (CSs), were analysed for grain-size distribution. For this purpose, we relied on a

196 Malvern Mastersizer 3000 equipped with a Hydro SV dispersion unit. To ensure
197 reproducibility, each sample was analysed five times (Malvern Panalytical, 2015).

198

199 **3.3. Chronology**

200

201 Age control for the core DST-2023 GC was established using radiocarbon (^{14}C) dating, with
202 samples taken near distinct (unit) transitions, as identified by visual logging and core imagery
203 (see the previous section). The extracted material was then wet-sieved using 250 μm and 125
204 μm meshes, examined, and picked under a Leica MZ6 light microscope at magnifications of
205 6.3-40x, then dried overnight at 50°C. To reduce freshwater reservoir effects (Philippsen,
206 2013), we prioritised terrestrial plant macrofossils. Their selection was based solely on
207 preserved morphological features (vascular plant fragments, such as leaves and stems, and
208 seeds). However, because we could collect only three samples of terrestrial plant material, we
209 also collected four samples of aquatic moss. We paired them with terrestrial material in two
210 same-depth intervals and one adjacent interval because the dry weights of the terrestrial
211 fragments were low (Table 1), and to also screen for potential hardwater effects. The material
212 was submitted for Accelerator Mass Spectrometer (AMS) dating, with six samples sent to the
213 Poznań Radiocarbon Laboratory in Poland (Poz) in December 2023 (Goslar et al., 2004), and
214 one to the Tandem Laboratory at Uppsala University in Sweden (Ua; Table 1) in October 2024.

215

216 We established chronological control for the ~120.5 cm-long DST-2023-GC record by
217 generating an age-depth model, based on seven AMS ^{14}C dates (Fig. 2B; Table 1). We used the
218 Bayesian Bacon R package v.3.3.1 (Blaauw et al., 2022), calibrated ^{14}C ages using the IntCal20
219 Northern Hemisphere calibration curve (Reimer et al., 2020), and reported a 2σ (95%)

220 confidence range (cal. yrs B.P.; Fig. 2A, Table 1). The core top was assigned a zero age (2023
221 C.E. – the year of core extraction).

222

223 **3.4. Statistics**

224

225 Since the core compressed by ~5 cm during CT scanning in an upright position, we linearly
226 tuned the CT grayscale to previously measured DBD values, as both parameters reflect
227 sediment density (Fig. 3B; van der Bilt et al., 2018b), and the latter retained the original depth
228 scale. We standardised the data to z-scores before defining tie-points at major corresponding
229 trends and applied linear interpolation between tie-points using QAnalySeries software (Kotov
230 and Pälke, 2018). Next, we resampled the corrected CT grayscale values at a 500 μm in PAST
231 v. 4 (Hammer et al., 2001), consistent with the input resolution.

232

233 We only considered XRF elements with medium to high sensitivity to the fitted Cr tube and a
234 Signal-to-Noise ratio (SNR; μ/σ) ≥ 1 (Montgomery, 2017). We applied a centred-log ratio (clr)
235 transformation to remove closed-sum effects and minimise matrix-related artefacts (e.g.,
236 variability in water content, grain-size, porosity, and organic matter), allowing statistical
237 comparison of inter-element relationships and robust identification of sediment sources
238 (Bertrand et al., 2024). The transformation was performed in the CoDaPack software (Thió-
239 Henestrosa and Comas, 2011).

240

241 Grain-size statistics, expressed as metric (μm) Folk and Ward values, were calculated using the
242 GRADISTAT software (Blott and Pye, 2001). We then applied End Member Modelling
243 Analysis (EMMA) to unmix particle size distributions and disentangle eolian sediment sources

244 (Paterson and Heslop, 2015; Prins and Weltje, 1999), using AnalySize v. 1.2.2 in MATLAB
245 (Paterson and Heslop, 2015). We employed the non-parametric HALS-NMF algorithm because
246 it is well-suited for grain-size unmixing and disentangling depositional processes, and
247 reproduces the physically meaningful and plausible End Members (EMs; Paterson and Heslop,
248 2015). To ground-truth our EMs, we measured grain-size in catchment samples (CS 1-4) and
249 tested whether their distributions matched the EM modes.

250

251 To enable statistical analyses on a shared 0.5 cm resolution with physical measurements, XRF
252 and CT grayscale data were smoothed (using 25- and 10-point moving averages, respectively),
253 then resampled in PAST v. 4 (Hammer et al., 2001). Using the same software, we first
254 calculated Spearman's rank correlation coefficients (ρ), then applied cross-correlations (r) to
255 address potential offsets between physical measurements and scanning data. Previously,
256 EMMA-derived EMs were transformed to the logarithm (log), following the recommendations
257 of Bertrand et al. (2024). We then examined the shared gradients of change among selected
258 proxy parameters in the DST-2023 GC using Principal Component Analysis (PCA). The
259 analysis was performed on the following variables: CT grayscale, DBD, LOI, clr Fe, Ti, and
260 Ca, and log EM 1-3 abundances, with the input data standardised beforehand, following the
261 PAST v. 4 manual (Hammer et al., 2001).

262

263 **3.5. Scanning Electron Microscopy and Energy Dispersive X-ray Spectroscopy**

264

265 We used Scanning Electron Microscopy (SEM) to obtain high-resolution images of the
266 sediment matrix, authigenic phases and individual clastic grains, including their surface features
267 (Itamiya et al., 2019; Marshall et al., 2012; Vos et al., 2014). We also used Energy-Dispersive

268 X-ray Spectroscopy (SEM-EDS) to map and quantify elemental and oxide compositions at the
269 grain level (Newbury and Ritchie, 2015).

270

271 Overall, we examined 12 downcore samples and two catchment samples (CSs) representing the
272 Eastern inlet (CS 1), and the Western alluvial plain (CS 2; see also ‘Study area’ and Figs. 1D;
273 S1A-C). Initially, to identify the main lithological variability and obtain SEM imagery, we
274 collected five bulk sediment samples (10.5, 36.5, 80.5, 104.5, and 113.5 cm; 1 ml each) from
275 each key lithological unit (see our ‘Stratigraphy and geochemistry’ section). Next, to test the
276 EMMA- and XRF-based provenance interpretation at the grain-size scale, we also targeted six
277 samples containing leftover material from grain-size measurements (8.5, 79.5, 81.5, 82.5,
278 116.5, and 117.5 cm) and one from the vegetation mat at a depth of 1.5 cm, along with CSs 1-
279 2. These samples were separated into two size fractions prior to analysis, to characterise grain-
280 size compositional and morphological properties relevant to potential provenance: the <20 μm
281 material was used to assess the elemental composition and morphology of clastic carbonates,
282 while the >20 μm material was targeted to map oxide compositions and morphology of Fe-Ti-
283 rich clasts. In both cases, SEM-EDS spectra were collected from individual grains.

284

285 All samples were prepared at the EARTHLAB facility at UiB and analysed at the ELMILAB,
286 UiB. Before analysis, we dried bulk sediment samples for 12 hours at 50°C. Leftover material
287 from grain-size analysis was additionally sonicated in distilled water for 60 s, filtered through
288 20 μm polycarbonate membranes mounted in 5 ml Eppendorf tubes, and then dried under the
289 same conditions as bulk sediment samples. All samples were mounted on aluminium stubs with
290 adhesive carbon (C) tape and coated using an Agar Turbo Carbon Coater.

291

292 We used a ZEISS SUPRA 55VP SEM equipped with a Thermo Scientific Noran System 7 EDS
293 with Pathfinder X-ray Microanalysis software v. 2.11. SEM-EDS and SEM imagery of the <20
294 μm fraction were conducted under high-vacuum conditions at 15 kV, a working distance of
295 ~ 8.5 mm, and a dwell lifetime of 30 s for EDS analyses. For the imagery, we selected a
296 secondary electron (SE2) detector, and magnifications ranging from $\sim 3,000$ to $\sim 21,000$. To
297 improve surface resolution and reduce charging artefacts, the >20 μm fraction and bulk samples
298 were imaged at an accelerating voltage of 5 kV and with a working distance of ~ 5.8 -6.0 mm.
299 We also excluded C and oxygen (O) via manual deselection in Pathfinder v. 2.11 for all EDS
300 analyses, and converted the results to oxides (wt%).

301
302 To compare our oxides with the dolerite oxide record from Kapp Thordsen (CS-23) and
303 Gåsøyane (CS-24; Nejbort et al., 2011), we only targeted clasts in the >20 μm fraction that fell
304 within the $\pm 2\sigma$ grain-size window of EM 3 (the coarse-silt EM interpreted as eolian component
305 in this study – see section 4.3) to restrict the SEM-EDS comparison to grains most
306 representative of that EM, and therefore avoid biasing by different fractions. This retained 24%
307 of the initially mapped clasts and limited the focus to 59 spectra (typically 5-6 per clast). We
308 then normalised both wt% datasets to a common subset: Na_2O , MgO , Al_2O_3 , SiO_2 , P_2O_5 , K_2O ,
309 CaO , TiO_2 , MnO , and Fe_2O_3 . Because the reference dataset reports total Fe only as Fe_2O_3
310 (Nejbort et al., 2011) while we obtained only FeO, we calculated Fe_2O_3 values by multiplying
311 FeO concentrations by a stoichiometric factor of 1.111 (Element — Oxide Conversions, 2023).

312

313 **3.6. Mapping**

314

315 All spatial analyses were performed in QGIS 3.34 (Nyall Dawson et al., 2026), including
316 bathymetry post-processing and generating isobaths. We used ArcticDEM at 2 m resolution
317 (Porter et al., 2023) after correcting the offset between ellipsoid and geoid heights for altitude-
318 related calculations. The same tool was used to quantify the hypsometry of mapped dolerite
319 outcrops (Fig. 1C), with the areal extent of 5 m altitude bins calculated separately for Gåsøyane
320 and Gipshuksletta (3.5 km²), and for the combined area including Kapp Thordsen (13.4 km²).
321 A high-resolution orthophotography of Dunsappietjørna and its surroundings was processed
322 using a DJI Mavic 3E drone equipped with a Real Time Kinematic Global Navigation Satellite
323 System (RTK GNSS) module, following the workflow presented by Strzelecki et al. (2026).
324 The locations of the main geological units were obtained from the Norwegian Polar Institute
325 server (NPI Svalbardkartet, 2026), as were the background orthoimage and vector topography
326 shapefiles.

327

328 **4. Results and discussion**

329 **4.1. Core chronology**

330

331 Constrained by four accelerator mass spectrometry (AMS) ¹⁴C dates, the Bayesian age-depth
332 model reveals that the recovered sequence spans the last ca. 8,200 cal. yrs B.P. (the Mid- and
333 Late Holocene). Three anomalously young ages relative to their stratigraphic positions are
334 identified as outliers (Fig. 2A, Table 1). We exclude the risk of offsets associated with the
335 freshwater reservoir effect (Philippsen, 2013). Instead, as field observations and drone imagery
336 document soft vegetation mats across much of the lake bottom, including the coring site (Fig.
337 1E), we infer contamination by modern aquatic plant material (observed as dense soft mats

338 during the fieldwork in March 2024). During gravity coring, these mats were likely folded
339 against the liner walls and dragged upward as the barrel penetrated the sediments.

340

341 Based on core logging and Computed Tomography (CT) orthoslices, we did not observe marine
342 macrofossils, erosive contacts or rip-up clast or other macroscopic signs of marine influence in
343 the recovered sequence (Goslin and Clemmensen, 2017), consistent with the local sea-level
344 history and suggesting the timing of lake isolation to at least ca. 10,700 cal. yrs B.P. (see our
345 ‘Study area’; Forman et al., 2004; Lulák et al., 2026; Salvigsen, 1984; Strzelecki et al., 2026).
346 With our modelled basal age at ca. 8,200 cal. yrs B.P., this indicates that at least 2,500 yrs of
347 the earliest postglacial sediments were not retrieved (Fig. 2C).

348

349 SAR peaks at ~ 0.27 mm/yr between ca. 8,200-7,000 cal. yrs B.P. (Fig. 2B), overlapping with
350 the early phase of the Mid- Holocene deceleration in relative sea-level (RSL) fall reconstructed
351 from the adjacent Bjonasletta beach-ridge plain (Fig. 1B), which documents three major phases
352 of Holocene RSL regression (Fig. 2C; Strzelecki et al., 2026). Our observations are consistent
353 with higher sediment supply during catchment adjustment following deglaciation. Around ca.
354 7,000 cal. yrs B.P., SAR drops sharply and remains lower thereafter, consistent with reduced
355 changes in basin-shoreline geometry and slower RSL fall (Forman et al., 2004; Salvigsen, 1984;
356 Strzelecki et al., 2026).

357

358 **4.2. The Mid- and Late Holocene evolution of Dunsappietjørna**

359 **4.2.1. Core stratigraphy**

360

361 The Dunsappietjørna core comprises dark-brown, homogeneous, fine-grained sediments with
362 light-beige, fine-grained laminae that range in thickness from ~ 1.5 -2 mm to ~ 1 -2 cm. We

363 designate three main lithological units (1-3; Fig. 3), and use a change in laminae thickness and
364 resolution, shown in CT orthoslices and RGB imagery, to define the boundary between units 3
365 and 2, which coincides with a shift in lithogenic elemental values, expressed by centred-log
366 ratios (clr) of titanium (Ti), iron (Fe), and calcium (Ca). We also observe a more subtle shift in
367 lamina thickness and resolution concurrent with changes in lithogenic elemental values between
368 units 2 and 1, accompanied by a marked change in organic content (Loss On Ignition, LOI, %;
369 Dean, 1974; Heiri et al., 2001). We further subdivide units 3 and 1 into subunits a-b (Fig. 3),
370 based on finer-scale variations in lamination and lamina thickness, shifts in the relationship
371 between clr Ti-Fe and clr Ca, as well as changes in organic content and sediment density.
372 Principal Component Analysis (PCA) supports this unit classification, with samples clustering
373 within the unit boundaries in the PCA ordination space (Fig. 4). Units are then contextualised
374 by the regional and local records of Mid- and Late Holocene climate variability. We also note
375 two distinct dark intervals at the depths of ~91.5-96.5 cm, and ~0-2.5 cm, both characterised
376 by high LOI and low density (Fig. 3B). Corresponding to vegetation mats on the lake bottom
377 (see the 'Core chronology'), they are excluded from further interpretations.

378

379 While Mean Grain-Size (MGS, μm) is dominated by medium-silt throughout the whole core,
380 End Member Modelling Analysis (EMMA) reveals three End Members (EMs; Dietze et al.,
381 2022; Paterson and Heslop, 2015; Prins and Weltje, 1999): medium-silt-sized EMs 1-2 ($\mu=9$,
382 and $16 \mu\text{m}$, respectively), and coarse-silt EM 3 ($\mu=27 \mu\text{m}$; Figs. 3B-C and S4B). Clr Ti – a
383 robust proxy for terrigenous material – is closely tracked by clr Fe (Fig. 3B; Auer et al., 2025;
384 Stachowska et al., 2024). This is consistent with a shared minerogenic control and supported
385 by their strong positive correlation ($\rho=0.89$; $p\leq 0.05$; $n=2,278$; Table 2 and Fig. S3). Both are
386 also moderately correlated with MGS ($\rho=0.49, 0.44$, respectively; $p\leq 0.05$; $n=112$), and CT
387 grayscale ($\rho=0.54, 0.30$; $p\leq 0.05$; $n=2,260$), and they also exhibit statistically significant but

388 weak to moderate correlation with EM 3 ($\rho=0.33, 0.40$, respectively; $p\leq 0.05$; $n=109$).
389 Additionally, EM 3 grain-size distribution resembles that of catchment sample (CS) 2, sourced
390 from the alluvial plain West of the lake (see Figs. 1E and 3C, as well as the ‘Study area’, and
391 ‘Methods’). SEM imagery and SEM-EDS reveal Ti- and Fe-rich minerogenic phases $>20\ \mu\text{m}$
392 in size, selected to minimise influence from neighbouring EM 2 and coarser clasts. With sizes
393 of $\sim 23\text{-}31\ \mu\text{m}$, all grains fall within the $\pm 2\sigma$ grain-size window of EM 3, and likely include
394 rutile (TiO_2), augite (clinopyroxene), and chlorite (hydrous phyllosilicate; Fig. 5E-H and Table
395 S3). However, because Fe is redox-sensitive (Bertrand et al., 2024; Davies et al., 2015;
396 Kylander et al., 2011), we cannot rule out a non-detrital component of its variability, reflected
397 in the $\log(\text{Fe}/\text{Ti})$ ratio (Fig. S5; Bertrand et al., 2024). Meanwhile, clr Ca reflects mixed
398 carbonate deposition, as SEM imagery and SEM-EDS identify both authigenic (Fig. 5A-B) and
399 clastic carbonates (Fig. 5C-D; Table S3). We associate the authigenic component with seasonal
400 in-lake precipitation that occurs during hardwater whiting conditions – a phenomenon most
401 pronounced in summer, when rising water temperatures reduce calcite solubility, promoting
402 precipitation (see also ‘Supplementary Note 2’; K uchler-Krischun and Kleiner, 1990; Mazurek
403 et al., 2012; Ohlendorf and Sturm, 2001). Located on carbonate-rich bedrock, Tundra Lakes in
404 Petuniabukta ($\sim 30\ \text{km}$ Northwest of Dunsappietj rna) exhibit peak summer water temperatures
405 exceeding 10°C (July-August), and pH conditions that favour calcite precipitation. As Tundra
406 Lakes provide a local analogue for conditions that can favour seasonal carbonate precipitation
407 in cold, hardwater lakes (Mazurek et al., 2012), we infer a similar mechanism in
408 Dunsappietj rna. We also observe that clr Ca is not linked to minerogenic control in the same
409 way as clr Ti-Fe , as indicated by their anticorrelation ($\rho=-0.94$ and -0.95 , respectively; $p\leq 0.05$;
410 $n=2,278$). It also anticorrelates with EM 3 ($\rho=-0.42$, $p\leq 0.05$, $n=109$) but shows a weak positive
411 correlation with both EM 1 ($\rho=0.21$, $p\leq 0.05$, $n=111$) and 2 ($\rho=0.22$, $p\leq 0.05$, $n=110$). Given the
412 predominance of carbonate rocks in the local bedrock (Brekke and Hansson, 1990; Dallmann,

413 2015), we test the presence of clastic carbonates in our core record. SEM imagery and SEM-
414 EDS reveal clastic dolomite and calcite crystals $<20\ \mu\text{m}$ in size (Fig. 5C-D and Table S3),
415 corresponding to most of the $\pm 2\sigma$ grain-size range of EM 2. We also note that EM 2 grain-size
416 distribution bears resemblance to that of CS 1 (Figs. 3C and S6), collected from the clayey-
417 silty, carbonate-rich Eastern inlet to the lake that is active during the melt season (see also
418 ‘Study area’, and Figs. 1D-E and S1A-B). Meanwhile, we tie EM 1 abundance to SEM-
419 identified authigenic carbonate phases. Without microfacies characterisation or an independent
420 annual chronology and seasonal markers, we do not interpret laminations in our lake record as
421 varves, even though varved lake sediments form when depositional processes are strongly
422 seasonal, and laminae are preserved under sustained absence of sediment mixing, e.g., under
423 limited wave reworking and bioturbation (Zolitschka et al., 2015). Consistent with best
424 practices outlined by Zolitschka et al. (2015), an annual signal cannot be established from visual
425 lamination alone and requires independent verification with complementary evidence.
426 Accordingly, we interpret the co-occurrence of carbonate phases and light laminae in our lake
427 archive as most likely consistent with short-duration hardwater precipitation pulses during the
428 ice-free season. In contrast, the more minerogenic, higher-density background could also
429 accommodate detrital runoff carbonate input. However, the current dataset does not
430 discriminate whether individual laminae reflect recurring seasonal processes or event
431 deposition, and we therefore treat lamination frequency as an indicator of depositional
432 variability rather than a sign of annual lamination. Finally, the first two principal components
433 (PCs) summarize 71.47% of the total variance, with PC 1 and PC 2 explaining 37.94% and
434 33.53%, respectively. PC 1 is primarily defined by clr Ti, Fe, and Ca, whereas PC 2 is defined
435 by LOI, log EM 2, DBD and CT grayscale (Fig. 4; Table S1).

436

437 **4.2.2. Climate controls on sedimentation**

438

439 Basal unit 3, divided into subunits 3b and 3a, covers 121.44-96.5 cm (Fig. 3). Spanning ca.
440 8,200-7,300 cal. yrs B.P., the unit covers the transition from the Early to the Mid- Holocene.
441 This is coeval with the highest SAR in Dunsappietjørna archive, which declines in step with
442 local RSL fall (Fig. 2B-C; Strzelecki et al., 2026). Light-beige sediments show high LOI and
443 clr Ca values but limited clastic and dense input. Along with the finest MGS and the highest
444 EM 1 abundance, this is consistent with enhanced authigenic carbonate and organic
445 sedimentation (Figs. 3B-C and S4B), supported by SEM imagery and SEM-EDS evidence for
446 flake-like, anhedral carbonates (Fig. 5B and Table S3). This proxy combination suggests that
447 unit 3 records a late phase of the Holocene Thermal Maximum (HTM), overlapping with the
448 regional glacier minimum ca. 8,000-6,000 cal. yrs. B.P. (Farnsworth et al., 2020), and warmer-
449 than-present conditions in alkenone-inferred lake records from Northern Svalbard shown in Fig.
450 7F (van der Bilt et al., 2019; Kong et al., 2025), while also being partly in-phase with the first
451 major Mid- Holocene cooling step between ca. 7,800-7,000 cal. yrs B.P. (van der Bilt et al.,
452 2018a). Regional hydroclimate reconstructions from Northern Svalbard further indicate winter-
453 dominated precipitation until ca. 6,000 cal. yrs B.P, under enhanced moisture supply and
454 reduced sea-ice influence (Kjellman et al., 2020), the latter documented in both local and
455 regional records, in Isfjorden and Fram Strait (Fig. 7D-E; Müller et al., 2012a, b and Rasmussen
456 et al., 2012). Thus, we infer that ca. 8,200-7,300 cal. yrs B.P., due to these boundary conditions,
457 Dunsappietjørna repeatedly approached carbonate supersaturation during the open-water and
458 melt seasons, with runoff likely delivering hardwater enriched in ions from the local bedrock
459 (Brekke and Hansson, 1990; Dallmann, 2015). This mechanism is consistent with Ca and
460 bicarbonate (HCO_3) enrichment reported in the hydrochemistry of Tundra Lakes and is
461 associated with solute delivery during seasonal runoff (Mazurek et al., 2012). It further meets
462 the expectation that increased precipitation (including winter snowfall) can amplify melt-season

463 runoff and discharge signals in lacustrine archives (Auer et al., 2025). It also remains consistent
464 with leaf-wax hydrogen isotope ($\delta^2\text{H}$) evidence for generally warm but unstable regional
465 hydroclimate between ca. 9,500-7,500 cal. yrs B.P. (Balascio et al., 2018), along with winter-
466 dominated precipitation persisting until ca. 6,000 cal. yrs B.P. (Kjellman et al., 2020).

467

468 Underlined by ~5 cm thick vegetation mat, unit 2 spans 91.5-54.5 cm and covers most of the
469 Mid- Holocene, from ca. 7,000 to 4,500 cal. yrs B.P (Figs. 2B and 3). SAR drops markedly
470 relative to unit 3 (Fig. 2B), and the sediments record a shift toward higher clastic delivery
471 superimposed on an authigenic carbonate component. We also report a drop in organic content,
472 suggesting a stepwise shortening of the open-water season. This shift is coeval with the end of
473 the first major Mid-Holocene cooling, terminating ca. 7,000 cal. yrs B.P. (van der Bilt et al.,
474 2018a), then the onset of progressive temperature decline from ca. 6,500 cal. yrs B.P. (Kong et
475 al., 2025). While other regional studies note prevailing ice-distal conditions in much of the Mid-
476 Holocene (Farnsworth et al., 2020), local multiproxy fjord evidence indicates renewed glacial
477 influence in Sassen- and Tempelfjorden, including the growth of Tunabreen between ca. 6,000
478 and 4,000 cal. yrs B.P. (Forwick et al., 2010). In parallel, progressive cooling is reflected by a
479 steady increase in ice rafting and seasonal sea-ice influence, both locally in Isfjorden and in
480 Fram Strait (Fig. 7D-E; Müller et al., 2012a, b and Rasmussen et al., 2012), shortening the
481 open-water season and reducing the duration of in-lake carbonate precipitation. In DST-2023-
482 GC, the growing input of Ti- and Fe-rich phases in the EM 3 grain-size window matches CS 2
483 from the Western alluvial plain (Figs. 3B-C, 5F-H and Tables S3-4). We also note that although
484 laminae are less frequent, they are thicker, and the authigenic clr Ca component remains within
485 a similar range to that in unit 3 (Fig. 3), as SEM imagery and SEM-EDS show flake-like,
486 anhedral authigenic carbonates in the unit's samples (Fig. 5A), similar to those reported in
487 Mazurek et al. (2012). We infer that hardwater enrichment and seasonal in-lake carbonate

488 precipitation likely persisted as in unit 3, sustained by continued solute delivery from carbonate
489 weathering during melt-season runoff, but became diluted by rising Fe-Ti-rich minerogenic
490 input from the West. This suggests that the shift from unit 3 to unit 2 reflects not the
491 disappearance of carbonate precipitation but rather a growing detrital overprint under cooler,
492 increasingly ice-affected conditions. We also note that the early part of unit 2, ca. 7,000-6,000
493 cal. yrs B.P. overlaps with winter-precipitation dominance inferred from $\delta^2\text{H}$ data (Kjellman et
494 al., 2020), after which the seasonality signal becomes less clear.

495

496 Unit 1 comprises the uppermost 54.5-2.5 cm of the record, is divided into two subunits: 1b and
497 1a, and is overlain by a modern ~2.5 cm-thick vegetation mat (Fig. 3). Spanning the last ca.
498 4,500 yrs, it covers the end of the Mid- and the entirety of the Late Holocene (Fig. 2A).
499 Sedimentation in Dunsappietjørna becomes progressively more detrital, coinciding with the
500 second alkenone-inferred cooling step ca. 4,400-4,300 cal. yrs B.P. (van der Bilt et al., 2018a),
501 followed by regional Neoglacial cooling (from ca. 4,200 cal. yrs B.P. onwards; Fig. 7F; van der
502 Bilt et al., 2018a; Kong et al., 2025), and renewed glacier activity on Svalbard (Farnsworth et
503 al., 2020). Unit 1 sediments are the darkest and, following an initial drop in density and clr Ti
504 and Fe, show a sustained increase coupled with grain coarsening, contrasted by a steady LOI
505 decline and generally lower clr Ca for most of the sequence (Figs. 3B-C and S4B). However,
506 while initially dominated by EM 3 associated with clastic input from the West, EM 2
507 progressively increases and dominates the upper part of 1b and the entire 1a (Figs. 3B and S4B).
508 A similar increase is observed in clr Ca. Moreover, from ca. 1,200 cal. yrs B.P., it broadly
509 coincides with the onset of peak glacial activity in the region (Farnsworth et al., 2020), and is
510 coeval with a decrease in clr Ti-Fe, as expressed by dense, light-beige lamination and a low rise
511 in SAR (Figs. 2B and 3). Unlike in unit 3, this Ca peak is not accompanied by elevated LOI or
512 EM 1 (Figs. 3B and S4B), suggesting it does not reflect renewed dominance of in-lake

513 hardwater precipitation. SEM imagery and SEM-EDS reveal slightly rounded, subhedral
514 dolomite and calcite crystals in both core material and CS 1 samples (Figs. 5C-D, S6A-B, and
515 Table S3), hinting at growing fluvial delivery of carbonate-bearing medium-silt from the
516 seasonal Eastern inlet draining the Aitkenfjellen and Dalkallen side of the catchment during
517 summer snowmelt and rainfall-driven runoff (Figs. 1D and S1C). The uppermost sequences of
518 the core also overlap with more icy conditions in Isfjorden and increased sea-ice influence in
519 Fram Strait (Fig. 7D-E; Müller et al., 2012a, b and Rasmussen et al., 2012). Overall, the clastic
520 nature of unit 1 is consistent with Neoglacial boundary conditions that reduce authigenic in-
521 lake production due to a shorter open-water window, while enhancing the contribution of
522 minerogenic input from both Western and Eastern sources.

523

524 **4.3. Mid- to Late Holocene Westerly wind input**

525

526 The nearest largest mapped Fe- and Ti-rich lithologies are dolerite outcrops located West and
527 Northwest of the lake, in Gåsøyane, Gipshuksletta, and Kapp Thordsen (see also Fig. 1C, and
528 ‘Study area’; NPI Geological maps, 2026; Brekke and Hansson, 1990; Nejbort et al., 2011;
529 Senger et al., 2014; A. M. R. Sartell – personal communication). Out of the selected SEM-EDS
530 oxide compositions of Fe-Ti-rich clasts within the $\pm 2\sigma$ grain-size window of EM 3, 69% (41
531 out of 59 spectra) yielded dolerite-indicative compositions, defined here as spectra that fall
532 within or closely overlap the published major-oxide compositions reported for dolerites from
533 Kapp Thordsen (CS-23) and Gåsøyane (CS-24; Nejbort et al., 2011), supporting a local dolerite
534 source for the targeted clasts (see also our ‘Methods’). Additional dolerite-indicative spectra
535 not illustrated in Fig. 5 (and Table S3) are listed in Table S4.

536

537 RSL reconstructions from inner Isfjorden show rapid postglacial emergence from the marine
538 limit, followed by a deceleration in the RSL fall after ca. 8,000-7,000 cal. yrs B.P. (Fig. 2C; see
539 also 4.1; Strzelecki et al., 2026). Combined with the local topography (Fig. 1C), these
540 reconstructions indicate that the dolerite outcrops around Gåsøyane, Gipshuksletta and Kapp
541 Thordsen were at least partly emergent and therefore available as subaerial sources throughout
542 the deposition of our record (Fig. 6A-B). Using the data from Bjonasletta beach-ridge system
543 as a local analogue, RSL at ca. 8,000 cal. yrs B.P. was ~22 m a.s.l. (Fig. 2C; Strzelecki et al.,
544 2026). This implies that ~51.9% of the mapped dolerite outcrop area in Gåsøyane and
545 Gipshuksletta, and ~13.6% when including Kapp Thordsen, could be submerged at that time
546 (Fig. 6B and Table S5). Thus, the availability of dolerite-derived material likely increased as
547 RSL fell, particularly during the early part of the record (Figs. 2C and 6B). This time-varying
548 exposure possibly explains the strength of the Fe-Ti-rich signal and, apart from the factors
549 discussed in section 4.2.1, is a probable reason for the lower clr Ti-Fe values in older unit 3 (see
550 also ‘Supplementary Note 3’).

551
552 Local dolerite outcrops lie upwind of Dunsappietjørna under the dominant summer Westerlies
553 (Fig. 1B and Study area), consistent with reported valley-fjord wind channelling between the
554 study area and the Sassenfjorden sector (Frank et al., 2023a, b). Accordingly, we interpret
555 variability in EM 3 and its co-variation with clr Fe and Ti, captured by PC 1 (Fig. 4), as
556 reflecting changes in Westerly-driven eolian input from the local dolerite outcrops. In
557 periglacial settings, the expression of an eolian input is further controlled by seasonal
558 cryospheric barriers (snow, frozen ground, lake ice) that regulate the availability and mobility
559 of loose material for transport (Rasmussen et al., 2023; Rymer et al., 2022; Stachowska et al.,
560 2024). At our site, the ice-free season is ~3 months-long per year (see also ‘Study area’), but
561 reported dust mobilisation windows in Svalbard range from summer to late autumn-early winter

562 (Kavan et al., 2020; Meinander et al., 2022; Rasmussen et al., 2023; Rymer et al., 2022).
563 Nevertheless, local observations of dust deposition in Petuniabukta (Central Svalbard) show
564 that the largest dust events are commonly associated with the warm season, when surface
565 sediments are both snow-free and dry (Kavan et al., 2020). For quartz-density particles
566 matching the EM 3 mode and the targeted Ti-Fe grains (see section 4.2.1), the initiation of
567 motion remains threshold-limited, and it cannot be readily assessed as a simple linear wind-
568 speed threshold. Coarse-silt often enters short-term suspension upon release, but this emission
569 is usually caused by saltation impacts and sandblasting rather than by direct aerodynamic lift,
570 as cohesion prevents the direct entrainment of fine particles (Kok et al., 2012). Moreover,
571 effective mobilisation also depends strongly on surface moisture and the availability of saltating
572 coarser grains that can release finer fractions by sandblasting (Fécan et al., 1999; Kok et al.,
573 2012). Consequently, while we treat the variability captured by clr Fe-Ti and EM 3 as mainly
574 an ice-free, summer Westerly signal, its intensity and timing probably reflect the past frequency
575 of events that exceeded average seasonal thresholds and were further influenced by surface
576 conditions (dryness, sediment cohesion, and supply). We also cannot entirely rule out
577 occasional transport outside the peak summer season.

578

579 In this study, clr Fe has the strongest loading on PC 1 (Fig. 4 and Table S1), and is a diagnostic
580 component of dolerite-derived input. Therefore, we selected it as the primary high-resolution
581 proxy for summer Westerlies. We standardised clr Fe values to z-scores per unit and subunit to
582 assess variability while accounting for sedimentological and geochemical differences across
583 units (Toonen et al., 2015), particularly the non-stationary strength of dolerite-derived clasts.
584 To identify phases of intensified eolian activity, we highlighted all values at or above the 90th
585 percentile (*p*90) threshold (Hobday et al., 2016; Perkins-Kirkpatrick and Lewis, 2020),
586 calculated separately for each unit or subunit, accounting for unit- and subunit-specific

587 backgrounds (Figs. 7C and S7). While this eliminates baseline offsets caused by lithology and
588 time-varying source exposure, we interpret the resulting maxima as relative phases of
589 intensified Westerly winds rather than discrete events. This is also because the record predates
590 instrumental wind observations, and long archives often exhibit centennial-level chronological
591 uncertainties (Kylander et al., 2023; Stachowska et al., 2024), as reflected here by a mean 2σ
592 uncertainty of ca. 733 years (Figs. 2A, 7C, and S7). Clustering neighbouring maxima separated
593 by <400 yrs (more than a half of the mean 2σ uncertainty), we identify four Mid- and Late
594 Holocene phases of enhanced Westerly activity in the Dunsappietjørna archive between ca.
595 8,000-7,300 (phase I), 6,900-5,700 (phase II), 4,900-3,600 (phase III) and 1,200-1,000 (phase
596 IV) cal. yrs B.P. (Figs. 7C and S7).

597

598 **4.4. The Mid- and Late Holocene drivers of Westerly change**

599

600 Although broadly overlapping with the progressive cooling, unlike major shifts in
601 sedimentation, the four (I-IV) phases of Westerly maxima identified in our record are generally
602 not monotonic with Svalbard climate transitions (Fig. 7B-F), and the wind signal remains
603 comparatively stable through the recorded ca. 8,200 yrs. To contextualise major wind phases in
604 terms of boundary conditions that control or modulate sediment entrainment and deposition, we
605 compare them to local (Isfjorden) and regional Holocene-long records that resolve multi-
606 centennial variability in temperature, ice rafting, sea-ice, and glacial history. We do not treat
607 these variables as direct controls on wind strength but rather as boundary conditions that
608 influence near-surface stress, open-water exposure (Frank et al., 2025), sediment availability,
609 and the efficiency with which winds translate into eolian transport (Stachowska et al., 2024).
610 Accordingly, phase I (ca. 8,000-7,300 cal. yrs B.P.; Fig. 7C) occurs under an optimal but
611 transitional early Mid- Holocene background (Fig. 7F; Kong et al., 2025 and van der Bilt et al.,

612 2018a), aligning with the regional glacier minimum ca. 8,000-6,000 cal. yrs B.P. (Farnsworth
613 et al., 2020), yet also partly overlapping with the first major Mid- Holocene cooling step ca.
614 7,800-7,000 cal. yrs B.P. (van der Bilt et al., 2018a). This interval of enhanced wind activity in
615 the study area also falls within stepwise cooling in Isfjorden, ca. 8,200 and 7,400 cal. yrs B.P.,
616 linked to increased ice rafting, polar-water influence and seasonal sea-ice (Fig. 7D; Rasmussen
617 et al., 2012), as well as more persistent sea-ice conditions in the region, as shown by the Fram
618 Strait record (Fig. 7E; Müller et al., 2012a, b). This local progressive reduction in open-water
619 conditions is also consistent with a slowing in beach-ridge formation (Strzelecki et al., 2026).
620 Phase II (ca. 6,900-5,700 cal. yrs B.P.) is coeval with the onset of the regional cooling trend
621 (van der Bilt et al., 2018a; Kong et al., 2025), particularly from ca. 6,500 cal. yrs B.P. (Kong et
622 al., 2025), although following the end of the glacier minimum ca. 8,000 cal. yrs B.P.,
623 Farnsworth et al. (2020) report uneven regional constraints on glacier conditions until ca. 4,500
624 cal. yrs B.P., contrasted by the growth of local Tunabreen between ca. 6,000-4,000 cal. yrs B.P.
625 (Forwick et al., 2010). Similar to phase I, our second phase of Westerly maxima is coeval with
626 the increasing ice rafting and sea-ice influence (Müller et al., 2012a, b; Rasmussen et al., 2012),
627 and with a further drop in the Bjonasletta's beach-ridge progradation (Strzelecki et al., 2026).
628 Both phases I-II are therefore expressed despite an evolving polar-water regime, consistent with
629 the interpretation that the warm-season Westerly signal can peak under both relatively mild and
630 progressively cooler backgrounds. Phase III (ca. 4,900-3,600 cal. yrs B.P.) shows that enhanced
631 Westerly input overlaps the second major alkenone-inferred Mid- Holocene cooling step, ca.
632 4,400-4,300 cal. yrs B.P. (van der Bilt et al., 2018a), then spans the Neoglacial (from ca. 4,200
633 cal. yrs B.P.), and the onset of episodic glacier expansion after ca. 4,000 cal. yrs B.P.
634 (Farnsworth et al., 2020). It is also in phase with the stepwise cooling in Isfjorden that precedes
635 minimum bottom-water temperatures between ca. 4,000 and 2,000 cal. yrs B.P. under
636 strengthened polar water and sea-ice influence (Rasmussen et al., 2012), reducing wave

637 exposure and further slowing the beach-ridge progradation (Strzelecki et al., 2026). Local fjord
638 studies further suggest glacier advances around Sassen- and Tempelfjorden coeval with phase
639 III (Forwick et al., 2010). Phase IV (ca. 1,200-1,000 cal. yrs B.P.) occurs within the cold Late
640 Holocene mean state marked by a further drop in spring and summer temperatures (van der Bilt
641 et al., 2018a; Kong et al., 2025), with enhanced wind activity shortly overlapping with the
642 regional peak glacier activity ca. 1,000-500 cal. yrs. B.P. (Farnsworth et al., 2020). However,
643 while regional records suggest increased sea-ice cover (Müller et al., 2012a, b), the Isfjorden
644 shows progressively less stable bottom-water conditions following episodic warmer Atlantic
645 Water (AW) inflows after ca. 2,000 cal. yrs B.P. (Rasmussen et al., 2012). Forwick et al. (2010)
646 also document local heterogeneity through multiple glacier-front advances and retreats over the
647 past two millennia. Overall, our record does not show additional sustained clusters of Westerly
648 maxima through much of the Late Holocene, between ca. 3,600-1,200 and after ca. 1,000 cal.
649 yrs B.P. (Figs. 7C and S7). This suggests reduced clastic input under colder, generally more
650 ice-affected boundary conditions in which longer seasonal ice cover and stronger cryogenic
651 barriers shorten the effective depositional window, and more persistent sea-ice reduces near-
652 surface coupling and open-water exposure. At the same time, we again emphasise that our
653 Westerly maxima do not show a monotonic response to climate shifts, as none of the several
654 milder episodes associated with AW inflows into Isfjorden in the last two millennia is
655 accompanied by values exceeding the $p90$ threshold (Fig. 7C-D; Rasmussen et al., 2012). Taken
656 together, we infer that in the DST-2023 GC record, the depositional expression of Westerlies
657 depended on the interaction of atmospheric forcing with changing exposure, cryogenic barriers,
658 and sediment availability.

659

660 To place the Dunsappietjørna record into a broader Svalbard paleo wind context, we compare
661 it with the Steinbruvatnet record from Southern Svalbard (Fig. 7B-C; Stachowska et al., 2024).

662 Both lacustrine archives isolate multi-centennial variability in warm-season elastic input
663 attributed to the Westerlies and are reconstructed using comparable high-resolution multiproxy
664 methods (Stachowska et al., 2024). However, the Southern Svalbard record resolves the wind
665 maxima between ca. 9,700 and 1,700 cal. yrs B.P. (Stachowska et al., 2024), whereas
666 Dunsappietjørna – although lacking the Early Holocene context – extends High Arctic Westerly
667 wind behaviour to the present. Beyond the difference in temporal coverage, there is a
668 fundamental contrast in setting: while Dunsappietjørna lies in an inner-fjord environment,
669 Steinbruvatnet is located in an exposed coastal sector, capturing a more direct expression of
670 ocean-atmosphere dynamics in the North Atlantic (Stachowska et al., 2024). We note that the
671 similarity between Westerly maxima in the Central and Southern Svalbard records is observable
672 only between ca. 8,200 and 5,700 cal. yrs B.P. (phases I-II of our record, Fig. 7B-C), with little
673 overall correspondence thereafter. Chronological offsets are plausible because both archives
674 exhibit centennial-scale age uncertainties (Stachowska et al., 2024). Moreover, misalignments
675 are expected in multi-centennial storm reconstructions – with storminess here defined as wind
676 strength and wave height after Stachowska et al. (2024) – because proxy and site responses can
677 diverge even when shifts in storminess are broadly similar, including variability within a
678 sequence and across a wider (~100 km) transect (Kylander et al., 2023). Kylander et al. (2023)
679 further argue that lateral shifts in storm track position can result in strong spatial gradients, with
680 sites adjacent to the storm track responding differently from those at its margins.

681

682 Although paleo data are limited in the study area, modern wind observations reveal considerable
683 spatial heterogeneity in both surface wind direction and magnitude relative to the open coast,
684 as shown in Fig. S8 (Frank et al., 2023a, b, 2025; MET Norway, 2026). These patterns are
685 largely driven by valley-fjord orientation, headland speed-up zones, and land-sea thermal
686 contrast (Frank et al., 2023a, b, 2025). The closest available inner-fjord observations for our

687 study area are from the Isfjorden-Gåsøyane station, which began full operations only in 2025
688 (MET Norway, 2026). Such a short record cannot resolve longer-term trends and only hints at
689 a seasonal cycle in wind direction and strength. Nevertheless, in 2025, Westerly winds (SW,
690 WSW, W, WNW, NW) accounted for ~21% of annual observations, peaking at ~63% of all
691 measured winds in July and of maximum gale speed (≤ 17.1 m/s). The JJA wind roses from
692 other Isfjorden stations further show that directional regimes and high-wind classes vary
693 strongly across the fjord system (Fig. S8; MET Norway, 2026), consistent with local
694 topographic steering, as highlighted by Frank et al. (2025). At Gåsøyane, Southwest-Northwest
695 winds account for ~39.4% of JJA observations, but winds of ≥ 10.7 m/s speed (fresh breeze or
696 stronger) are more frequent from North-Northeast and East-Southeast than from Western-
697 Northwestern directions. Further air-sea measurements by Frank et al. (2025) suggest that in
698 Isfjorden, sea-ice conditions play a first-order control on near-surface air-sea coupling and on
699 the efficiency with which winds are expressed over open-water, and show that even modest
700 sea-ice can reduce the air-sea temperature contrast and shorten open-water exposure, weakening
701 surface winds despite potentially strong flow aloft. This sensitivity is also consistent with
702 observations showing that surface drag can peak at intermediate sea-ice concentrations due to
703 form drag from floe edges, and is strongly dependent on ice morphology and floe size (Elvidge
704 et al., 2016; Lüpkes and Birnbaum, 2005).

705

706 As previously mentioned in section 4.3, a further implication is that the delivery of EM 3-sized
707 (coarse-silt) eolian fraction could likely be disproportionately influenced by episodic high-wind
708 events associated with cyclones passing over the archipelago, rather than by average
709 background wind flow. In the modern Arctic, summer cyclones can be linked to brief periods
710 of extreme near-surface winds and increased surface wind stress, including that over sea-ice
711 (Croad et al., 2023; Tanaka et al., 2012). Preferred cyclone track corridors and cyclone types

712 can also impose spatial gradients in cyclone occurrence and intensity, as well as in associated
713 wind extremes (Croad et al., 2023). Because Arctic cyclone behaviour is linked to the
714 distribution of lower-tropospheric temperature gradients and sea-ice extent (Simmonds and
715 Rudeva, 2014), Holocene changes in insolation and boundary conditions at the ocean-ice
716 margin can plausibly modulate storm track positions and pathways in the North Atlantic (Orme
717 et al., 2017). Case observations from Fram Strait show that cyclones generated at the marginal
718 ice zone can propagate NNE along the ice edge and produce short-lived (several-hour) winds
719 exceeding 20 m/s (Brümmer et al., 2003). On the other hand, even when winds ≥ 20 m/s are
720 treated as a practical indicator of Arctic cyclone-strength winds, following Fram Strait
721 observations by Brümmer et al. (2003), wind rose data provide little direct support for such a
722 regime within Isfjorden (Fig. S8). This is also consistent with other modern observations from
723 Western Spitsbergen showing that wind-speed extremes depend strongly on circulation, with
724 the largest positive wind-speed anomalies occurring during Southwestern-Southern air-mass
725 advection (Araźny et al., 2022). At the same time, summertime (JJA) winds of ≥ 10.7 m/s occur
726 at several Isfjorden stations, including Gåsøyane, suggesting that threshold-exceeding winds
727 may be a realistic modern analogue for coarse-silt mobilisation even in the absence of a clear
728 cyclone-strength signal. In that framework, we cannot dismiss the possibility that small shifts
729 in past cyclone or storm track positions may still have altered the frequency of winds exceeding
730 entrainment thresholds that can mobilise coarse-silt, thereby influencing the variability of the
731 Fe-Ti-rich dolerite-derived input. At the same time, we want to emphasise that the data do not
732 justify directly identifying the observed JJA high-wind regimes in the study area with cyclones.

733

734 Overall, we use modern observations to evaluate the plausibility of wind steering and exposure
735 contrasts, and interpret the transfer of regional circulation variability to eolian sediment delivery
736 as nonlinear and highly site-dependent in inner-fjord settings. This approach aligns with the

737 limited correlation with Steinbruvatnet outside phases I-II (Stachowska et al., 2024), the
738 plausibility of centennial-scale chronological offsets (Kylander et al., 2023), and the
739 expectation that coarse-silt delivery responds disproportionately to wind events exceeding the
740 grain entrainment threshold. We also acknowledge that the expression of these patterns likely
741 varied throughout the Mid- and Late Holocene. Accordingly, the Dunsappietjørna archive is
742 most likely locally filtered due to valley-fjord wind steering, a sea-ice-limited fetch and
743 exposure, and time-varying sediment availability and deposition. If true, this may explain why
744 our inner-valley-fjord setting does not directly reflect the open-coastal patterns of increased
745 wind activity during regional cooling phases (Stachowska et al., 2024), and why major regional
746 transitions might either not be shown or are highly muted or phase-shifted. However, our record
747 also does not support the view that a warmer, less icy Arctic will be stormier due to stronger
748 surface winds, longer fetch, and enhanced wave activity (Casas-Prat and Wang, 2020; Li et al.,
749 2019; Mioduszewski et al., 2018). Instead, Dunsappietjørna provides a high-resolution inner-
750 fjord perspective on High Arctic eolian variability over the last ca. 8,200 yrs and reinforces the
751 need for spatial transects and multi-site comparisons when synthesising storm reconstructions
752 across Svalbard.

753

754 **5. Conclusions**

755

756 This study shows that inner-fjord lake sediments can preserve a high-resolution eolian record
757 over centennial timescales, provided that local topographic filtering and complex boundary
758 conditions are systematically accounted for. Our results suggest that isolating eolian signals in
759 such settings is most effective when employing an integrated multiproxy toolbox that couples
760 high-resolution core scanning with grain-specific provenance validation.

761

762 The primary contribution of this work is the application of a workflow that bridges macro-scale
763 stratigraphy and micro-scale mineralogy. By integrating XRF and CT scanning with End
764 Member Modelling Analysis (EMMA), we identify a coarse-silt component indicative of wind-
765 driven transport. Critically, we validate this eolian signal using Scanning Electron Microscopy
766 and Energy Dispersive X-ray Spectroscopy (SEM-EDS) to map and geochemically fingerprint
767 Fe-Ti-rich minerogenic phases. This allows us to link the sediment to specific dolerite outcrops
768 located West of the basin, providing a diagnostic provenance target that distinguishes eolian
769 clastic input from other parallel depositional processes.

770

771 Applying this toolbox to Dunsappietjørna, we resolve four multi-centennial phases of enhanced
772 eolian activity over the past ca. 8,200 yrs, and show how inner-fjord-valley geometry and time-
773 varying sediment availability modulate the regional atmospheric signal. Our findings indicate
774 that while Dunsappietjørna likely captures broader Holocene wind trends, the magnitude of the
775 depositional response in this sheltered inner-fjord setting is heavily filtered by local boundary
776 conditions and sediment supply. Accordingly, the record does not support a simple monotonic
777 relationship between either colder or warmer conditions and stronger winds at this site.

778

779 On a regional scale, the scarcity and varied sensitivity of Arctic wind archives make direct
780 comparisons challenging. To improve the comparability of these records, we advocate for the
781 wider adoption of this provenance-validated workflow. Future research should apply this
782 multiproxy approach along spatial transects – from exposed coastal sites to sheltered inner-fjord
783 valleys – to better constrain how complex topography filters atmospheric forcing, as we believe
784 that such high-resolution, validated archives are essential for understanding how Arctic
785 warming will continue to reshape wind patterns, sea-ice extent, and post-glacial sediment
786 dynamics.

787

788 **Acknowledgements**

789

790 This research received funding from the Polish National Science Centre (NCN) grant *ASPIRE*
791 – *Arctic storm impacts recorded in beach-ridges and lake archives: scenarios for less icy future*
792 (No. UMO-2020/37/B/ST10/03074), led by M.C.S. (PI) and W.v.d.B. (Co-PI). W.v.d.B.'s
793 contribution was additionally supported by a *Starting Grant* from the Trond Mohn Research
794 Foundation (TMF; No. TMS2021STG01). In 2024, Z.S. received a mobility grant from *HarSval*
795 *Bilateral initiative aiming at a Harmonisation of the Svalbard cooperation and activities*
796 *funding from the means of the EEA and Norway Grants 2014-2021* (No. UMO-
797 2023/43/7/ST10/00001), as well as the Doctoral School of the University of Szczecin's Grant
798 for scientific development, which both supported her mobility to Bergen and Longyearbyen. In
799 2025, Z.S.'s research activity was further supported by the Ministry of Science and Higher
800 Education's *Regional Excellence Initiative Programme* (No. 3/D/2025) and the Foundation for
801 Polish Science (FNP) *Start Programme*. We sincerely thank Andreea G. Auer (A.G.A.) for
802 sharing her expertise in multivariate statistics. We also thank Irene Heggstad for dedicating her
803 time and knowledge to Scanning Electron Microscopy (SEM) and Energy-Dispersive X-ray
804 Spectroscopy (SEM-EDS), as well as for assisting with additional technical questions. For the
805 latter, we are also grateful to Harald Hausen. Our thanks go to Haflidi Haflidason for his
806 feedback on the stratigraphy and for his tips on mapping dolerite clasts using SEM and SEM-
807 EDS. We also appreciate Danuta Cembrowska-Lech for providing polycarbonate membranes
808 and for advice on their use in sample preparation. We thank Jan Magne Cederstrøm for
809 performing the Computed Tomography (CT) scan and providing his recommendations to
810 correct the compressed CT grayscale values. We express our gratitude to Pål T. Mørkved for
811 granting access to the weighing room and microbalance in the Facility for advanced isotopic

812 research and monitoring of weather, climate and biogeochemical cycling (FARLAB) at the
813 University of Bergen, which helped us assess the most stable readings of radiocarbon samples.
814 We extend our sincere appreciation to Kim Senger and Anna M. R. Sartell for sharing data and
815 their expertise in mineralogy and petrography of local dolerites. Lastly, we thank all our
816 colleagues who, along with A.G.A., participated in the fieldwork: Chris Hein, Sebastian
817 Lindhorst, Joseph M. Buckby, Knut I. L. Tveit, and Peter Betlem.

818

819 **Author contributions statement**

820

821 W.v.d.B. and M.C.S. secured funding for this study. The study design and methodology were
822 primarily developed by W.v.d.B. and implemented by Z.S., with contributions from I.H.T.,
823 W.v.d.B., M.C.S., J.K., and M.F.A.F. W.v.d.B., M.C.S., J.K., Z.S., and M.F.A.F. participated
824 in the fieldwork and conducted sediment sampling. Z.S. wrote the original draft, and all authors
825 contributed to its final version. Figures were produced by Z.S. and J.K.

826

827 **Competing Interests statement**

828

829 The authors declare no competing interests.

830

831 **Data availability**

832

833 The authors declare that all data generated from the sediment core DST-2023 GC for this study,
834 and presented in its figures and tables (including the Supplementary Information file), have

835 been made available in the DataverseNO repository, where the files can be accessed under the
836 following link: doi:10.18710/K3CDJJ. Source data generated in this study are also provided
837 with this paper as an .xls file, with a separate sheet for each figure and table.

838

839 **References**

840

841 Arażny, A., Przybylak, R., and Kejna, M.: The Influence of Atmospheric Circulation on Mean
842 and Extreme Weather Conditions on Kaffiøyra (NW Spitsbergen, Svalbard Archipelago) in
843 the Summer Seasons 1975–2015, *Front. Environ. Sci.*, 10, 867106,
844 <https://doi.org/10.3389/fenvs.2022.867106>, 2022.

845 Auer, A. G., Van Der Bilt, W. G. M., Schomacker, A., Bakke, J., Støren, E. W. N., Buckby, J.
846 M., Cederstrøm, J. M., and Van Der Plas, S.: Hydroclimate intensification likely aided glacier
847 survival on Svalbard in the Early Holocene, *Commun Earth Environ*, 6, 100,
848 <https://doi.org/10.1038/s43247-025-02064-z>, 2025.

849 Balascio, N. L., D’Andrea, W. J., Gjerde, M., and Bakke, J.: Hydroclimate variability of High
850 Arctic Svalbard during the Holocene inferred from hydrogen isotopes of leaf waxes,
851 *Quaternary Science Reviews*, 183, 177–187, <https://doi.org/10.1016/j.quascirev.2016.11.036>,
852 2018.

853 Bertrand, S., Tjallingii, R., Kylander, M. E., Wilhelm, B., Roberts, S. J., Arnaud, F., Brown,
854 E., and Bindler, R.: Inorganic geochemistry of lake sediments: A review of analytical
855 techniques and guidelines for data interpretation, *Earth-Science Reviews*, 249, 104639,
856 <https://doi.org/10.1016/j.earscirev.2023.104639>, 2024.

- 857 van der Bilt, W. G. M., D'Andrea, W. J., Bakke, J., Balascio, N. L., Werner, J. P., Gjerde, M.,
858 and Bradley, R. S.: Alkenone-based reconstructions reveal four-phase Holocene temperature
859 evolution for High Arctic Svalbard, *Quaternary Science Reviews*, 183, 204–213,
860 <https://doi.org/10.1016/j.quascirev.2016.10.006>, 2018a.
- 861 van der Bilt, W. G. M., Rea, B., Spagnolo, M., Roerdink, D. L., Jørgensen, S. L., and Bakke,
862 J.: Novel sedimentological fingerprints link shifting depositional processes to Holocene
863 climate transitions in East Greenland, *Global and Planetary Change*, 164, 52–64,
864 <https://doi.org/10.1016/j.gloplacha.2018.03.007>, 2018b.
- 865 van der Bilt, W. G. M., D'Andrea, W. J., Werner, J. P., and Bakke, J.: Early Holocene
866 Temperature Oscillations Exceed Amplitude of Observed and Projected Warming in Svalbard
867 Lakes, *Geophysical Research Letters*, 46, 14732–14741,
868 <https://doi.org/10.1029/2019GL084384>, 2019.
- 869 Blaauw, M., Christen [aut, J. A., ctb, cph, Lopez, M. A. A., Vazquez, J. E., V, O. M. G.,
870 Belding, T., Theiler, J., Gough, B., and Karney, C.: rbacon: Age-Depth Modelling using
871 Bayesian Statistics, 2022.
- 872 Blott, S. J. and Pye, K.: GRADISTAT: a grain size distribution and statistics package for the
873 analysis of unconsolidated sediments, *Earth Surf. Process. Landforms*, 26, 1237–1248,
874 <https://doi.org/10.1002/esp.261>, 2001.
- 875 Brekke, B. and Hansson, R.: Environmental atlas Gipsdalen, Svalbard. Vol. II, Reports on the
876 quaternary geology, vegetation, flora, and fauna of Gipsdalen, and the marine ecology of
877 Gipsvika, 1990.
- 878 Brooks, R. A. and Di Chiro, G.: Statistical limitations in x-ray reconstructive tomography,
879 *Medical Physics*, 3, 237–240, <https://doi.org/10.1118/1.594240>, 1976.

- 880 Brümmer, B., Müller, G., and Hoeber, H.: A Fram Strait cyclone: Properties and impact on
881 ice drift as measured by aircraft and buoys, *J. Geophys. Res.*, 108, 2002JD002638,
882 <https://doi.org/10.1029/2002JD002638>, 2003.
- 883 Casas-Prat, M. and Wang, X. L.: Projections of Extreme Ocean Waves in the Arctic and
884 Potential Implications for Coastal Inundation and Erosion, *JGR Oceans*, 125,
885 e2019JC015745, <https://doi.org/10.1029/2019JC015745>, 2020.
- 886 Chen, W. and Guillaume, M.: HALS-based NMF with flexible constraints for hyperspectral
887 unmixing, *EURASIP J. Adv. Signal Process.*, 2012, 54, [https://doi.org/10.1186/1687-6180-](https://doi.org/10.1186/1687-6180-2012-54)
888 2012-54, 2012.
- 889 Cnudde, V. and Boone, M. N.: High-resolution X-ray computed tomography in geosciences:
890 A review of the current technology and applications, *Earth-Science Reviews*, 123, 1–17,
891 <https://doi.org/10.1016/j.earscirev.2013.04.003>, 2013.
- 892 Cox Analytical System: Itrax Core Scanner: Q-Spec 6.5.2. Software Manual. Mölndal, 13 pp,
893 2008.
- 894 Croad, H. L., Methven, J., Harvey, B., Keeley, S. P. E., Volonté, A., and Hodges, K. I.: A
895 Climatology of Summer-Time Arctic Cyclones Using a Modified Phase Space, *Geophysical*
896 *Research Letters*, 50, e2023GL105993, <https://doi.org/10.1029/2023GL105993>, 2023.
- 897 Dallmann, W. K.: *Geoscience atlas of Svalbard*, Norsk Polarinstitut, 2015.
- 898 Davies, S. J., Lamb, H. F., and Roberts, S. J.: Micro-XRF Core Scanning in Palaeolimnology:
899 Recent Developments, in: *Micro-XRF Studies of Sediment Cores: Applications of a non-*
900 *destructive tool for the environmental sciences*, edited by: Croudace, I. W. and Rothwell, R.

- 901 G., Springer Netherlands, Dordrecht, 189–226, https://doi.org/10.1007/978-94-017-9849-5_7,
902 2015.
- 903 Dietze, M., Schulte, P., and Dietze, E.: Application of end-member modelling to grain-size
904 data: Constraints and limitations, *Sedimentology*, 69, 845–863,
905 <https://doi.org/10.1111/sed.12929>, 2022.
- 906 Elvidge, A. D., Renfrew, I. A., Weiss, A. I., Brooks, I. M., Lachlan-Cope, T. A., and King, J.
907 C.: Observations of surface momentum exchange over the marginal ice zone and
908 recommendations for its parametrisation, *Atmos. Chem. Phys.*, 16, 1545–1563,
909 <https://doi.org/10.5194/acp-16-1545-2016>, 2016.
- 910 Farnsworth, W. R., Allaart, L., Ingólfsson, Ó., Alexanderson, H., Forwick, M., Noormets, R.,
911 Retelle, M., and Schomacker, A.: Holocene glacial history of Svalbard: Status, perspectives
912 and challenges, *Earth-Science Reviews*, 208, 103249,
913 <https://doi.org/10.1016/j.earscirev.2020.103249>, 2020.
- 914 Fécan, F., Marticorena, B., and Bergametti, G.: Parametrization of the increase of the aeolian
915 erosion threshold wind friction velocity due to soil moisture for arid and semi-arid areas, *Ann.*
916 *Geophys.*, 17, 149–157, <https://doi.org/10.1007/s00585-999-0149-7>, 1999.
- 917 Førland, E. J., Benestad, R., Hanssen-Bauer, I., Haugen, J. E., and Skaugen, T. E.:
918 Temperature and Precipitation Development at Svalbard 1900–2100, *Advances in*
919 *Meteorology*, 2011, 1–14, <https://doi.org/10.1155/2011/893790>, 2011.
- 920 Forman, S. L., Lubinski, D. J., Ingólfsson, Ó., Zeeberg, J. J., Snyder, J. A., Siegert, M. J., and
921 Matishov, G. G.: A review of postglacial emergence on Svalbard, Franz Josef Land and
922 Novaya Zemlya, northern Eurasia, *Quaternary Science Reviews*, 23, 1391–1434,
923 <https://doi.org/10.1016/j.quascirev.2003.12.007>, 2004.

- 924 Forwick, M., Vorren, T. O., Hald, M., Korsun, S., Roh, Y., Vogt, C., and Yoo, K.-C.: Spatial
925 and temporal influence of glaciers and rivers on the sedimentary environment in
926 Sassenfjorden and Tempelfjorden, Spitsbergen, SP, 344, 163–193,
927 <https://doi.org/10.1144/SP344.13>, 2010.
- 928 Frank, L., Jonassen, M. O., Skogseth, R., and Vihma, T.: Atmospheric Climatologies Over
929 Isfjorden, Svalbard, JGR Atmospheres, 128, e2022JD038011,
930 <https://doi.org/10.1029/2022JD038011>, 2023a.
- 931 Frank, L., Jonassen, M. O., and Remes, T.: IWIN: The Isfjorden Weather Information
932 Network, <https://doi.org/10.21343/EBRW-W846>, 2023b.
- 933 Frank, L., Jonassen, M. O., Skogseth, R., and Vihma, T.: Air–sea–ice interactions in
934 Isfjorden, Svalbard: An atmospheric perspective, Quart J Royal Meteor Soc, 151, e4956,
935 <https://doi.org/10.1002/qj.4956>, 2025.
- 936 Goslar, T., Czernik, J., and Goslar, E.: Low-energy ¹⁴C AMS in Poznań Radiocarbon
937 Laboratory, Poland, Nuclear Instruments and Methods in Physics Research Section B: Beam
938 Interactions with Materials and Atoms, 223–224, 5–11,
939 <https://doi.org/10.1016/j.nimb.2004.04.005>, 2004.
- 940 Goslin, J. and Clemmensen, L. B.: Proxy records of Holocene storm events in coastal barrier
941 systems: Storm-wave induced markers, Quaternary Science Reviews, 174, 80–119,
942 <https://doi.org/10.1016/j.quascirev.2017.08.026>, 2017.
- 943 Hammer, O., Harper, D., and Ryan, P.: PAST: Paleontological Statistics Software Package for
944 Education and Data Analysis, Palaeontologia Electronica, 4, 1–9, 2001.

- 945 Hess, K., Engel, M., Patel, T., Vakhrameeva, P., Koutsodendris, A., Klemt, E., Hansteen, T.
946 H., Kempf, P., Dawson, S., Schön, I., and Heyvaert, V. M. A.: A 1500-year record of North
947 Atlantic storm flooding from lacustrine sediments, Shetland Islands (UK), *J Quaternary*
948 *Science*, jqs.3568, <https://doi.org/10.1002/jqs.3568>, 2023.
- 949 Hobday, A. J., Alexander, L. V., Perkins, S. E., Smale, D. A., Straub, S. C., Oliver, E. C. J.,
950 Benthuyssen, J. A., Burrows, M. T., Donat, M. G., Feng, M., Holbrook, N. J., Moore, P. J.,
951 Scannell, H. A., Sen Gupta, A., and Wernberg, T.: A hierarchical approach to defining marine
952 heatwaves, *Progress in Oceanography*, 141, 227–238,
953 <https://doi.org/10.1016/j.pocean.2015.12.014>, 2016.
- 954 Itamiya, H., Sugita, R., and Sugai, T.: Analysis of the surface microtextures and morphologies
955 of beach quartz grains in Japan and implications for provenance research, *Prog Earth Planet*
956 *Sci*, 6, 43, <https://doi.org/10.1186/s40645-019-0287-9>, 2019.
- 957 Kavan, J., Láska, K., Nawrot, A., and Wawrzyniak, T.: High Latitude Dust Transport Altitude
958 Pattern Revealed from Deposition on Snow, Svalbard, *Atmosphere*, 11, 1318,
959 <https://doi.org/10.3390/atmos11121318>, 2020.
- 960 Kjellman, S. E., Schomacker, A., Thomas, E. K., Håkansson, L., Duboscq, S., Cluett, A. A.,
961 Farnsworth, W. R., Allaart, L., Cowling, O. C., McKay, N. P., Brynjólfsson, S., and
962 Ingólfsson, Ó.: Holocene precipitation seasonality in northern Svalbard: Influence of sea ice
963 and regional ocean surface conditions, *Quaternary Science Reviews*, 240, 106388,
964 <https://doi.org/10.1016/j.quascirev.2020.106388>, 2020.
- 965 Kok, J. F., Parteli, E. J. R., Michaels, T. I., and Karam, D. B.: The physics of wind-blown
966 sand and dust, *Rep. Prog. Phys.*, 75, 106901, [https://doi.org/10.1088/0034-](https://doi.org/10.1088/0034-4885/75/10/106901)
967 [4885/75/10/106901](https://doi.org/10.1088/0034-4885/75/10/106901), 2012.

- 968 Kong, S.-R., Van Der Bilt, W. G. M., Mørkved, P. T., Wörmer, L., Hasal, K., and D'Andrea,
969 W. J.: Sub-centennially resolved reconstruction of surface temperature on High Arctic
970 Svalbard for the past 13,000 years, *Earth and Planetary Science Letters*, 671, 119646,
971 <https://doi.org/10.1016/j.epsl.2025.119646>, 2025.
- 972 Element — Oxide Conversions: <https://meteorites.wustl.edu/goodstuff/oxides.htm>, last
973 access: 26 November 2023.
- 974 Kotov, S. and Pälike, H.: QAnalySeries – a cross-platform time series tuning and analysis
975 tool, *Earth and Space Science Open Archive*, <https://doi.org/10.1002/essoar.10500226.1>,
976 2018.
- 977 Kylander, M. E., Ampel, L., Wohlfarth, B., and Veres, D.: High-resolution X-ray
978 fluorescence core scanning analysis of Les Echets (France) sedimentary sequence: new
979 insights from chemical proxies: XRF CORE SCANNING ANALYSIS OF LES ECHETS
980 SEDIMENTARY SEQUENCE, *J. Quaternary Sci.*, 26, 109–117,
981 <https://doi.org/10.1002/jqs.1438>, 2011.
- 982 Kylander, M. E., Martínez-Cortizas, A., Sjöström, J. K., Gåling, J., Gyllencreutz, R., Bindler,
983 R., Alexanderson, H., Schenk, F., Reinardy, B. T. I., Chandler, B. M. P., and Gallagher, K.:
984 Storm chasing: Tracking Holocene storminess in southern Sweden using mineral proxies from
985 inland and coastal peat bogs, *Quaternary Science Reviews*, 299, 107854,
986 <https://doi.org/10.1016/j.quascirev.2022.107854>, 2023.
- 987 Li, J., Ma, Y., Liu, Q., Zhang, W., and Guan, C.: Growth of wave height with retreating ice
988 cover in the Arctic, *Cold Regions Science and Technology*, 164, 102790,
989 <https://doi.org/10.1016/j.coldregions.2019.102790>, 2019.

- 990 Lulák, M., Nývlt, D., Novák, M., and Kavan, J.: Holocene relative sea level changes and their
991 consequences for the development of the palaeoshoreline in central Svalbard, Czech Polar
992 Rep., 15, 121–138, <https://doi.org/10.5817/CPR2025-S-7>, 2026.
- 993 Lüpkes, C. and Birnbaum, G.: ‘Surface Drag in the Arctic Marginal Sea-ice Zone: A
994 Comparison of Different Parameterisation Concepts,’ *Boundary-Layer Meteorol*, 117, 179–
995 211, <https://doi.org/10.1007/s10546-005-1445-8>, 2005.
- 996 Malvern Panalytical: Mastersizer 3000 User Manual English, 2015.
- 997 Marshall, J. R., Bull, P. A., and Morgan, R. M.: Energy regimes for aeolian sand grain surface
998 textures, *Sedimentary Geology*, 253–254, 17–24,
999 <https://doi.org/10.1016/j.sedgeo.2012.01.001>, 2012.
- 1000 Mazurek, M., Paluszkiewicz, R., Rachlewicz, G., and Zwoliński, Z.: Variability of Water
1001 Chemistry in Tundra Lakes, Petuniabukta Coast, Central Spitsbergen, Svalbard, *The*
1002 *Scientific World Journal*, 2012, 1–13, <https://doi.org/10.1100/2012/596516>, 2012.
- 1003 Meinander, O., Dagsson-Waldhauserova, P., Amosov, P., Aseyeva, E., Atkins, C., Baklanov,
1004 A., Baldo, C., Barr, S. L., Barzycka, B., Benning, L. G., Cvetkovic, B., Enchilik, P., Frolov,
1005 D., Gassó, S., Kandler, K., Kasimov, N., Kavan, J., King, J., Koroleva, T., Krupskaya, V.,
1006 Kulmala, M., Kusiak, M., Lappalainen, H. K., Laska, M., Lasne, J., Lewandowski, M., Luks,
1007 B., McQuaid, J. B., Moroni, B., Murray, B., Möhler, O., Nawrot, A., Nickovic, S., O’Neill, N.
1008 T., Pejanovic, G., Popovicheva, O., Ranjbar, K., Romanias, M., Samonova, O., Sanchez-
1009 Marroquin, A., Schepanski, K., Semenov, I., Sharapova, A., Shevnina, E., Shi, Z., Sofiev,
1010 M., Thevenet, F., Thorsteinsson, T., Timofeev, M., Umo, N. S., Uppstu, A., Urupina, D.,
1011 Varga, G., Werner, T., Arnalds, O., and Vukovic Vimic, A.: Newly identified climatically and

- 1012 environmentally significant high-latitude dust sources, *Atmos. Chem. Phys.*, 22, 11889–
1013 11930, <https://doi.org/10.5194/acp-22-11889-2022>, 2022.
- 1014 MET Norway: <https://seklima.met.no/>, last access: 2 January 2026.
- 1015 Mioduszewski, J., Vavrus, S., and Wang, M.: Diminishing Arctic Sea Ice Promotes Stronger
1016 Surface Winds, *J. Climate*, 31, 8101–8119, <https://doi.org/10.1175/JCLI-D-18-0109.1>, 2018.
- 1017 Montgomery, D. C.: *Design and Analysis of Experiments*, John Wiley & Sons, 752 pp., 2017.
- 1018 Mulwijk, M., Hattermann, T., Martin, T., and Granskog, M. A.: Future sea ice weakening
1019 amplifies wind-driven trends in surface stress and Arctic Ocean spin-up, *Nat Commun*, 15,
1020 6889, <https://doi.org/10.1038/s41467-024-50874-0>, 2024.
- 1021 Müller, J., Werner, K., Stein, R., Fahl, K., Moros, M., and Jansen, E.: Age determinations,
1022 biomarker analyses, and accumulation rates of three sediment cores from the Fram Strait, 6
1023 datasets, <https://doi.org/10.1594/PANGAEA.779628>, 2012a.
- 1024 Müller, J., Werner, K., Stein, R., Fahl, K., Moros, M., and Jansen, E.: Holocene cooling
1025 culminates in sea ice oscillations in Fram Strait, *Quaternary Science Reviews*, 47, 1–14,
1026 <https://doi.org/10.1016/j.quascirev.2012.04.024>, 2012b.
- 1027 Nejbert, K., Krajewski, K. P., Dubinska, E., and Pécskay, Z.: Dolerites of Svalbard, north-
1028 west Barents Sea Shelf: age, tectonic setting and significance for geotectonic interpretation of
1029 the High-Arctic Large Igneous Province, *Polar Research*, 30, 7306,
1030 <https://doi.org/10.3402/polar.v30i0.7306>, 2011.
- 1031 Newbury, D. E. and Ritchie, N. W. M.: Performing elemental microanalysis with high
1032 accuracy and high precision by scanning electron microscopy/silicon drift detector energy-

- 1033 dispersive X-ray spectrometry (SEM/SDD-EDS), *J Mater Sci*, 50, 493–518,
1034 <https://doi.org/10.1007/s10853-014-8685-2>, 2015.
- 1035 Nordli, Ø., Wyszynski, P., Gjeltten, H. M., Isaksen, K., Łupikasza, E., Niedźwiedź, T., and
1036 Przybylak, R.: Revisiting the extended Svalbard Airport monthly temperature series, and the
1037 compiled corresponding daily series 1898–2018, *Polar Research*, 39,
1038 <https://doi.org/10.33265/polar.v39.3614>, 2020.
- 1039 NPI Geological maps: <https://geokart.npolar.no/geologi/GeoSvalbard/#6/79.512/19.335>, last
1040 access: 12 February 2026.
- 1041 NPI Map Data and Services: <https://geodata.npolar.no/>, last access: 10 April 2025.
- 1042 NPI Svalbardkartet: <https://geokart.npolar.no/geologi/GeoSvalbard/#6/79.560/19.355>, last
1043 access: 18 February 2026.
- 1044 Nyall Dawson, Jürgen Fischer, Matthias Kuhn, Alessandro Pasotti, mhugent, Denis Rouzaud,
1045 Alexander Bruy, Tim Sutton, Martin Dobias, Mathieu Pellerin, Even Rouault, Víctor Olaya,
1046 Paul Blottiere, Werner Macho, Radim Blazek, Gary Sherman, Harrissou Sant-anna, Julien
1047 Cabieces, Loïc Bartoletti, Nathan Woodrow, signedav, rldhont, Stefanos Natsis, Larry
1048 Shaffer, Nedjima Belgacem, Sandro Santilli, Salvatore Larosa, Sandro Mani, Jean Felder, and
1049 Vincent Cloarec: *qgis/QGIS: 3.44.7*, , <https://doi.org/10.5281/ZENODO.6139224>, 2026.
- 1050 Orme, L. C., Charman, D. J., Reinhardt, L., Jones, R. T., Mitchell, F. J. G., Stefanini, B. S.,
1051 Barkwith, A., Ellis, M. A., and Grosvenor, M.: Past changes in the North Atlantic storm track
1052 driven by insolation and sea-ice forcing, *Geology*, 45, 335–338,
1053 <https://doi.org/10.1130/G38521.1>, 2017.

- 1054 Paterson, G. A. and Heslop, D.: New methods for unmixing sediment grain size data,
1055 *Geochemistry, Geophysics, Geosystems*, 16, 4494–4506,
1056 <https://doi.org/10.1002/2015GC006070>, 2015.
- 1057 Perkins-Kirkpatrick, S. E. and Lewis, S. C.: Increasing trends in regional heatwaves, *Nat*
1058 *Commun*, 11, 3357, <https://doi.org/10.1038/s41467-020-16970-7>, 2020.
- 1059 Philippsen, B.: The freshwater reservoir effect in radiocarbon dating, *herit sci*, 1, 24,
1060 <https://doi.org/10.1186/2050-7445-1-24>, 2013.
- 1061 Porter, C., Howat, I., Noh, M.-J., Husby, E., Khuvis, S., Danish, E., Tomko, K., Gardiner, J.,
1062 Negrete, A., Yadav, B., Klassen, J., Kelleher, C., Cloutier, M., Bakker, J., Enos, J., Arnold,
1063 G., Bauer, G., and Morin, P.: ArcticDEM - Mosaics, Version 4.1 (1.0),
1064 <https://doi.org/10.7910/DVN/3VDC4W>, 2023.
- 1065 Prins, M. A. and Weltje, G. J.: End-member modeling of siliciclastic grain-size distributions:
1066 The late Quaternary record of aeolian and fluvial sediment supply to the Arabian Sea and its
1067 paleoclimatic significance, in: *Numerical experiments in stratigraphy: Recent advances in*
1068 *stratigraphic and sedimentologic computer simulations*, edited by: Harbaugh, J., Society for
1069 *Sedimentary Geology*, 91–111, 1999.
- 1070 Rantanen, M., Karpechko, A. Y., Lipponen, A., Nordling, K., Hyvärinen, O., Ruosteenoja, K.,
1071 Vihma, T., and Laaksonen, A.: The Arctic has warmed nearly four times faster than the globe
1072 since 1979, *Commun Earth Environ*, 3, 1–10, <https://doi.org/10.1038/s43247-022-00498-3>,
1073 2022.
- 1074 Rasmussen, C. F., Christiansen, H. H., Buylaert, J.-P., Cunningham, A., Schneider, R.,
1075 Knudsen, M. F., and Stevens, T.: High-resolution OSL dating of loess in Adventdalen,

- 1076 Svalbard: Late Holocene dust activity and permafrost development, *Quaternary Science*
1077 *Reviews*, 310, 108137, <https://doi.org/10.1016/j.quascirev.2023.108137>, 2023.
- 1078 Rasmussen, T. L., Forwick, M., and Mackensen, A.: Reconstruction of inflow of Atlantic
1079 Water to Isfjorden, Svalbard during the Holocene: Correlation to climate and seasonality,
1080 *Marine Micropaleontology*, 94–95, 80–90, <https://doi.org/10.1016/j.marmicro.2012.06.008>,
1081 2012.
- 1082 Reimer, P. J., Austin, W. E. N., Bard, E., Bayliss, A., Blackwell, P. G., Ramsey, C. B.,
1083 Butzin, M., Cheng, H., Edwards, R. L., Friedrich, M., Grootes, P. M., Guilderson, T. P.,
1084 Hajdas, I., Heaton, T. J., Hogg, A. G., Hughen, K. A., Kromer, B., Manning, S. W.,
1085 Muscheler, R., Palmer, J. G., Pearson, C., Plicht, J. van der, Reimer, R. W., Richards, D. A.,
1086 Scott, E. M., Southon, J. R., Turney, C. S. M., Wacker, L., Adolphi, F., Büntgen, U., Capano,
1087 M., Fahrni, S. M., Fogtmann-Schulz, A., Friedrich, R., Köhler, P., Kudsk, S., Miyake, F.,
1088 Olsen, J., Reinig, F., Sakamoto, M., Sookdeo, A., and Talamo, S.: The IntCal20 Northern
1089 Hemisphere Radiocarbon Age Calibration Curve (0–55 cal kBP), *Radiocarbon*, 62, 725–757,
1090 <https://doi.org/10.1017/RDC.2020.41>, 2020.
- 1091 Røthe, T. O., Bakke, J., Støren, E. W. N., and Bradley, R. S.: Reconstructing Holocene
1092 Glacier and Climate Fluctuations From Lake Sediments in Vårfluesjøen, Northern
1093 Spitsbergen, *Frontiers in Earth Science*, 6, 2018.
- 1094 Rothwell, R. G. and Croudace, I. W.: Twenty Years of XRF Core Scanning Marine
1095 Sediments: What Do Geochemical Proxies Tell Us?, in: *Micro-XRF Studies of Sediment*
1096 *Cores: Applications of a non-destructive tool for the environmental sciences*, edited by:
1097 Croudace, I. W. and Rothwell, R. G., Springer Netherlands, Dordrecht, 25–102,
1098 https://doi.org/10.1007/978-94-017-9849-5_2, 2015.

- 1099 Rymer, K. G., Rachlewicz, G., Buchwal, A., Temme, A. J. A. M., Reimann, T., and Van Der
1100 Meij, W. M.: Contemporary and past aeolian deposition rates in periglacial conditions (Ebba
1101 Valley, central Spitsbergen), *CATENA*, 211, 105974,
1102 <https://doi.org/10.1016/j.catena.2021.105974>, 2022.
- 1103 Salvigsen, O.: Occurrence of pumice on raised beaches and Holocene shoreline displacement
1104 in the inner Isfjorden area, Svalbard, *Polar Research*, 2, 107–113,
1105 <https://doi.org/10.1111/j.1751-8369.1984.tb00488.x>, 1984.
- 1106 Saunders, K. M., Roberts, S. J., Perren, B., Butz, C., Sime, L., Davies, S., Van
1107 Nieuwenhuyze, W., Grosjean, M., and Hodgson, D. A.: Holocene dynamics of the Southern
1108 Hemisphere westerly winds and possible links to CO₂ outgassing, *Nature Geosci*, 11, 650–
1109 655, <https://doi.org/10.1038/s41561-018-0186-5>, 2018.
- 1110 Senger, K., Tveranger, J., Ogata, K., Braathen, A., and Planke, S.: Late Mesozoic magmatism
1111 in Svalbard: A review, *Earth-Science Reviews*, 139, 123–144,
1112 <https://doi.org/10.1016/j.earscirev.2014.09.002>, 2014.
- 1113 Simmonds, I. and Rudeva, I.: A comparison of tracking methods for extreme cyclones in the
1114 Arctic basin, *Tellus A: Dynamic Meteorology and Oceanography*, 66, 25252,
1115 <https://doi.org/10.3402/tellusa.v66.25252>, 2014.
- 1116 St. Louis, V. L., St. Pierre, K. A., Emmerton, C. A., Serbu, J. A., Talbot, C. H., Szostek, L.,
1117 Lehnerr, I., Muir, D. C. G., and Criscitiello, A.: Winter Dust Storms Impact the Physical and
1118 Biogeochemical Functioning of a Large High Arctic Lake, *Environ. Sci. Technol.*, 58, 7415–
1119 7424, <https://doi.org/10.1021/acs.est.4c00705>, 2024.

- 1120 Stachowska, Z., Van Der Bilt, W. G. M., and Strzelecki, M. C.: Coastal lake sediments from
1121 Arctic Svalbard suggest colder summers are stormier, *Nat Commun*, 15, 9688,
1122 <https://doi.org/10.1038/s41467-024-53875-1>, 2024.
- 1123 Strzelecki, M. C., Lindhorst, S., Hein, C. J., van der Bilt, W. G. M., Kivimaki, K. E., and
1124 Kavan, J.: 10,000 years of centennially-resolved climate and sea-level change archived in
1125 Svalbard beach-ridge system, *Sci Rep*, <https://doi.org/10.1038/s41598-025-33652-w>, 2026.
- 1126 Tanaka, H. L., Yamagami, A., and Takahashi, S.: The structure and behavior of the arctic
1127 cyclone in summer analyzed by the JRA-25/JCDAS data, *Polar Science*, 6, 55–69,
1128 <https://doi.org/10.1016/j.polar.2012.03.001>, 2012.
- 1129 Thió-Henestrosa, S. and Comas, M.: CoDaPack 2.0: a stand-alone, multi-platform
1130 compositional software, *Proceedings of CoDaWork'11: 4th international workshop on*
1131 *Compositional Data Analysis*, Egozcue, J.J., Tolosana-Delgado, R. and Ortego, M.I. (eds.)
1132 2011, Accepted: 2022-05-03T15:17:28Z, 2011.
- 1133 Toonen, W. H. J., Winkels, T. G., Cohen, K. M., Prins, M. A., and Middelkoop, H.: Lower
1134 Rhine historical flood magnitudes of the last 450years reproduced from grain-size
1135 measurements of flood deposits using End Member Modelling, *CATENA*, 130, 69–81,
1136 <https://doi.org/10.1016/j.catena.2014.12.004>, 2015.
- 1137 Vos, K., Vandenberghe, N., and Elsen, J.: Surface textural analysis of quartz grains by
1138 scanning electron microscopy (SEM): From sample preparation to environmental
1139 interpretation, *Earth-Science Reviews*, 128, 93–104,
1140 <https://doi.org/10.1016/j.earscirev.2013.10.013>, 2014.

1141 Zolitschka, B., Francus, P., Ojala, A. E. K., and Schimmelmann, A.: Varves in lake sediments
 1142 – a review, Quaternary Science Reviews, 117, 1–41,
 1143 <https://doi.org/10.1016/j.quascirev.2015.03.019>, 2015.

1144

1145 **Tables with captions**

1146

Lab code	Depth (cm)	Material	Dry weight (mg)	¹⁴ C age (yrs B.P.)	Error (¹⁴ C yrs)	Cal. yrs B.P.
Poz-173765	16.25	<i>Aquatic moss</i>	17	-602	25	-52 to -55
Poz-173976	16.25	<i>Terrestrial plants</i>	1.7	1,265	30	1,283 to 1,176
Poz-173973	53.75	<i>Aquatic moss</i>	5.3	4,010	30	4,529 to 4,415
Ua-85772	94	<i>Terrestrial plants</i>	1.6	6,352	49	7,339 to 7,165
Poz-173975	95	<i>Aquatic moss</i>	1.3	1,575	30	1,526 to 1,391
Poz-173974	117	<i>Aquatic moss</i>	12.3	-123	24	-66 to -69
Poz-173977	117	<i>Terrestrial plants</i>	1.1	7,150	40	8,020 to 7,930

1147 **Table 1. Radiocarbon sample overview.** All dating samples were extracted from the analysed
 1148 DST-2023 GC core. Calibrated ages, errors, and ranges (2σ) are based on the Intcal20 curve
 1149 (Reimer et al., 2020), and the calibration was performed using the Bayesian Bacon R package
 1150 v.3.3.1 (Blaauw et al., 2022). Gray text marks outliers.

1151

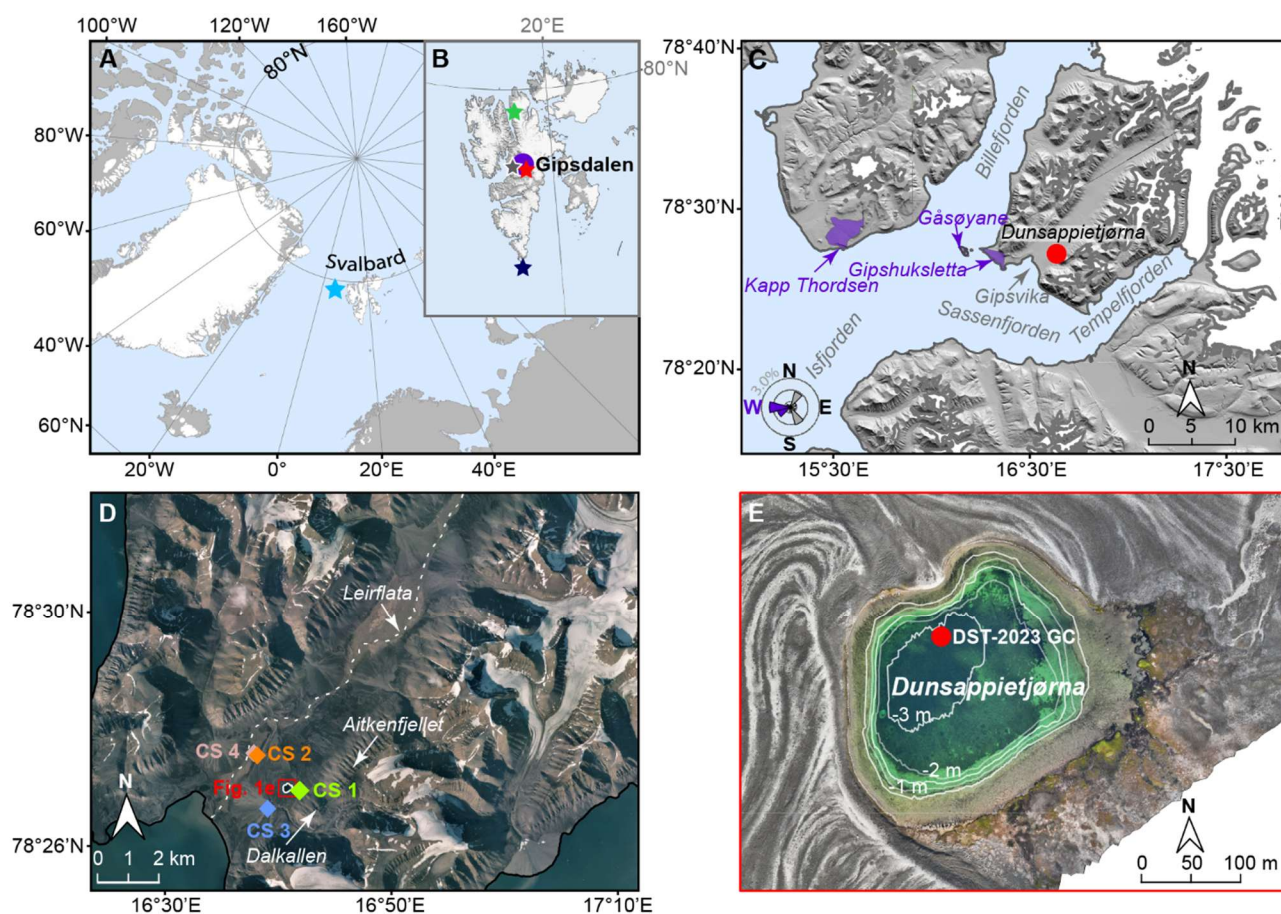
	CT	clr Ca	clr Ti	clr Fe	DBD	LOI	MGS	log EM 1	log EM 2
clr Ca	-0.33								
clr Ti	0.54	-0.94							
clr Fe	0.30	-0.95	0.89						
DBD	0.68	<i>0.14</i>	<i>0.05</i>	<i>-0.18</i>					
LOI	-0.67	<i>-0.13</i>	<i>-0.07</i>	<i>0.15</i>	-0.89				
MGS	0.38	-0.42	0.49	0.44	0.22	-0.22			
log EM 1	-0.49	0.21	-0.31	-0.24	-0.40	0.46	-0.83		
log EM 2	0.29	0.22	<i>-0.03</i>	<i>-0.15</i>	0.52	-0.61	<i>0.16</i>	-0.57	
log EM 3	<i>-0.01</i>	-0.42	0.33	0.40	<i>-0.18</i>	0.26	0.66	-0.27	-0.53

1152 **Table 2. Proxy correlations.** Black values reflect Spearman's correlation coefficients (ρ),
 1153 while gray values show cross-correlation between physical analyses and the resampled
 1154 scanning data (r). Values shown in italics reflect results with $p > 0.05$.

1155

1156 Figures with captions

1157

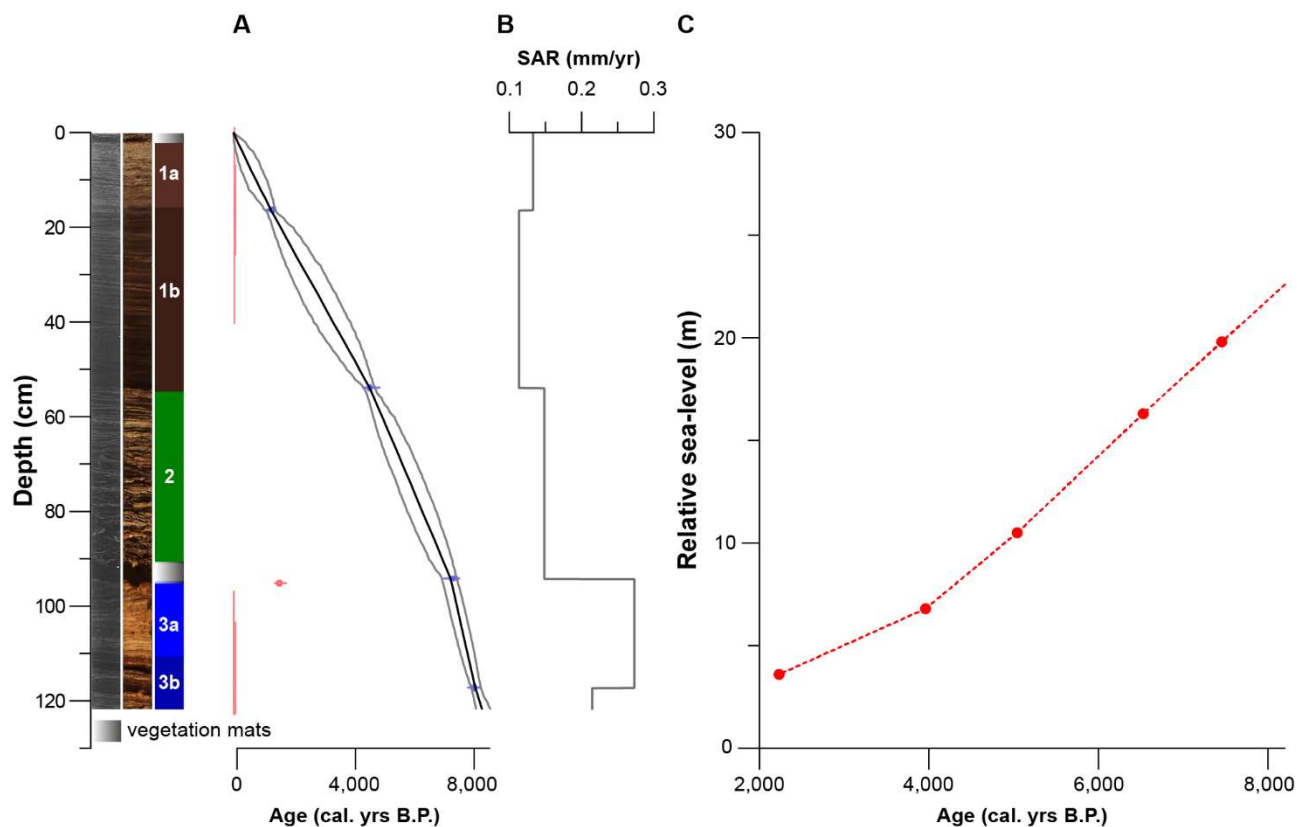


1158

1159 **Figure 1. Study area and site location.** A. Location of the Svalbard archipelago in a North
 1160 Atlantic-Arctic climate context. The light blue star marks the location of the P_{BIP25} -derived sea-
 1161 ice coverage data in Eastern Fram Strait (Müller et al., 2012a, b). B. Close-up of Svalbard,
 1162 showing the location of Gipsdalen (purple dot), Westerly wind reconstruction from
 1163 Steinbruvatnet (dark blue star; Stachowska et al., 2024); temperature anomalies from
 1164 Fiskedammane 3 – a closed lake in Northern Spitsbergen (green star; Kong et al., 2025), relative

1165 sea-level (RSL) curve from Bjonasletta beach-ridge plain in Central Spitsbergen (red star;
1166 Strzelecki et al., 2026), ice-rafted debris (IRD) data from core JM98-845-PC collected in
1167 Central Isfjorden (gray star with white outline; Rasmussen et al., 2012). **C.** ArcticDEM-derived
1168 topography illustrating valley-fjord meridional orientation (Porter et al., 2023), major fjords
1169 (gray labels), glaciers and ice caps (white), and key locations: the study site (red dot), as well
1170 as dolerite outcrops in Gipshuksletta, Gåsøyane, and Kapp Thordsen (outlined in purple;
1171 GeoSvalbard: NPI Geological maps, 2026; Brekke and Hansson, 1990; Nejbirt et al., 2011;
1172 Senger et al., 2014). The wind rose represents July-September wind direction data from the
1173 Gåsøyane lighthouse station (2023-2024; Frank et al., 2023b). **D.** Satellite imagery of the
1174 Dunsappietjørna catchment (NPI Map Data and Services, 2025), showing the locations of
1175 catchment samples (CSs 1-4), Leirflata floodplain, two mountains – Dalkallen and
1176 Aitkenfjellet, and Gipsdalselva (white dashed line). **E.** Drone imagery of Dunsappietjørna with
1177 bathymetry presented with 0.5 m contour isobaths (white lines). The location of the studied
1178 sediment core DST-2023 GC is highlighted in red.

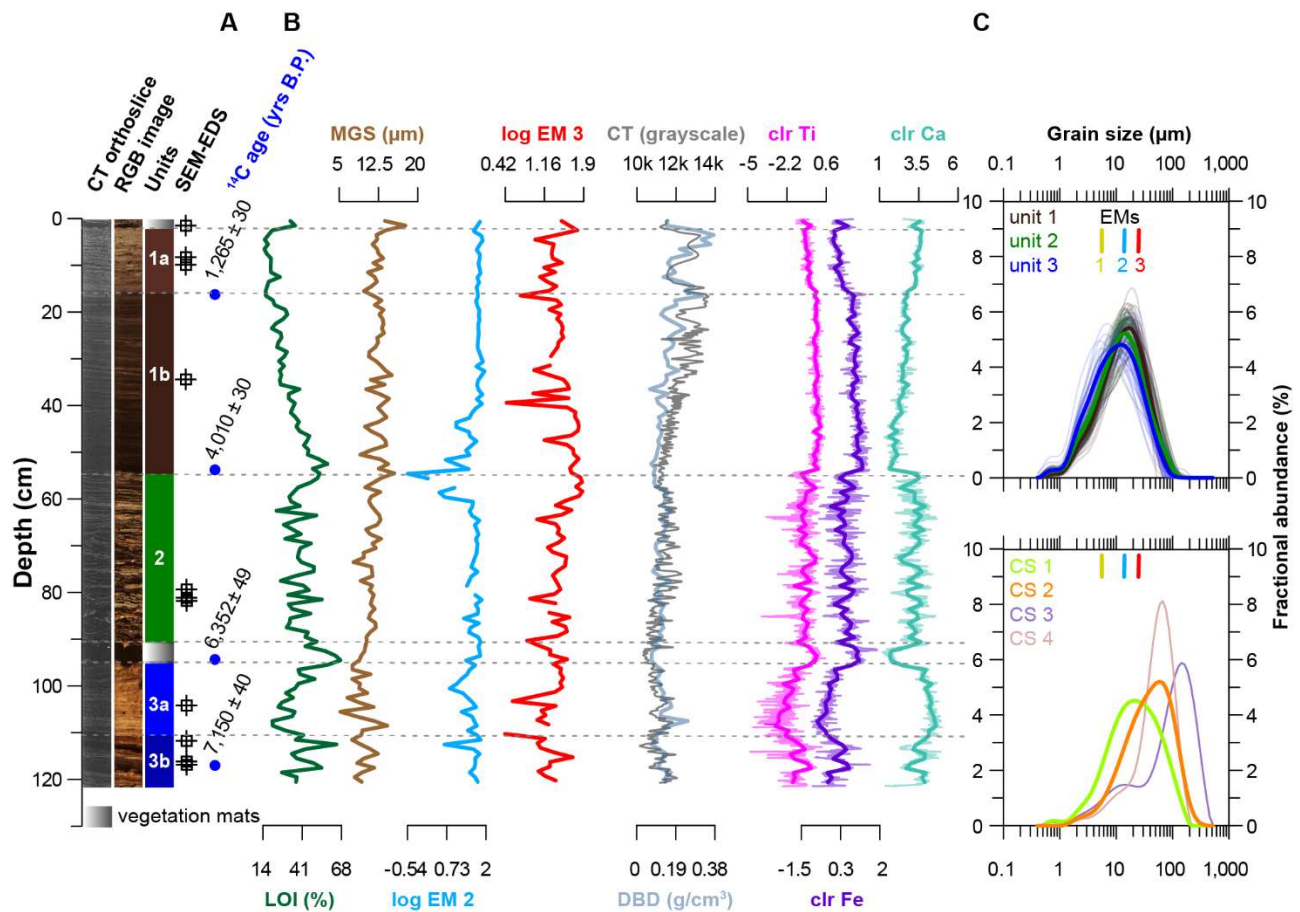
1179



1180

1181 **Figure 2. Chronology and sedimentation.** From the left: CT and optical imagery, and units-
 1182 subunits classification of the sedimentary record (see ‘The Mid- and Late Holocene evolution
 1183 of Dunsappietjørna’). **A.** Our age-depth model: the black line represents the weighted mean
 1184 best fit, while the gray lines depict the 95% confidence interval. Calibrated ^{14}C age distributions
 1185 are marked in blue (included), while red indicates anomalously young ages (outliers). **B.**
 1186 Sediment Accumulation Rate values (SAR; in mm/yr). **C.** Local RSL curve from Bjonasletta
 1187 beach-ridge plain in Central Spitsbergen (see also Fig. 1B; Strzelecki et al., 2026). We only
 1188 present the available timing coeval with our record.

1189



1190

1191 **Figure 3. Key proxies and grain-size statistics measured on Dunsappietjørna sediments.**

1192 From the left: CT and optical imagery, and unit-subunit classification of the sedimentary record.

1193 **A.** Position of samples selected for Scanning Electron Microscopy (SEM) imagery and Energy1194 Dispersive X-ray Spectroscopy (SEM-EDS; left), and position of ¹⁴C samples with ¹⁴C ages ±1195 errors (yrs; right). **B.** Organic content – shown by Loss on Ignition (LOI, %; Dean, 1974; Heiri

1196 et al., 2001), the grain-size variability – reflected by mean grain-size (MGS) values in µm, and

1197 logarithmic (log) ratios for the grain-size End Member Modelling (EMMA) output, reflected

1198 by End Members (EMs) 2 and 3 (Dietze et al., 2022; Prins and Weltje, 1999), density – captured

1199 by CT grayscale values shown on top (Cnudde and Boone, 2013), and Dry Bulk Density (DBD)

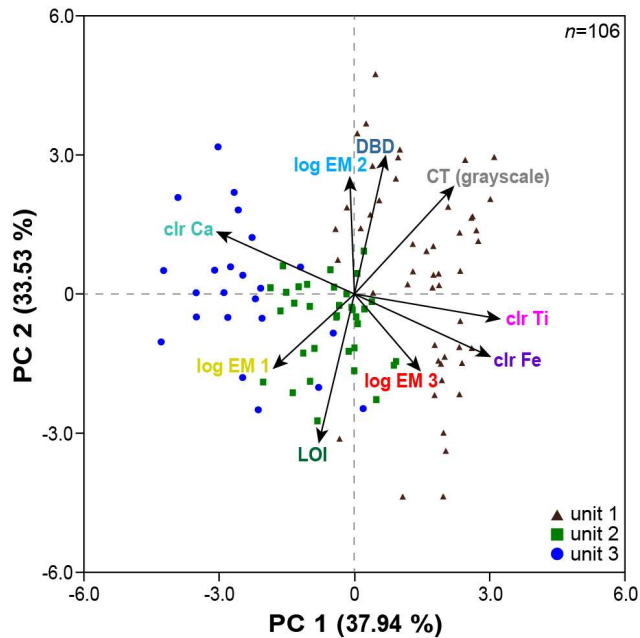
1200 shown on the bottom, minerogenic input – reflected by centred log-ratios (clr) of titanium (Ti;

1201 Auer et al., 2025; Stachowska et al., 2024), and iron (Fe; Bertrand et al., 2024; Davies et al.,

1202 2015), carbonate deposition – measured by clr calcium (Ca; Davies et al., 2015). **C.** The grain-1203 size distributions of samples from each unit ($n=121$), and colour-coded accordingly, with the

1204 unit mean curves highlighted in bold and the grain-size means of three EMs marked above
 1205 (top); CSs 1-4 (bottom; see also Figs. 1D and S1) – presented on a μm scale.

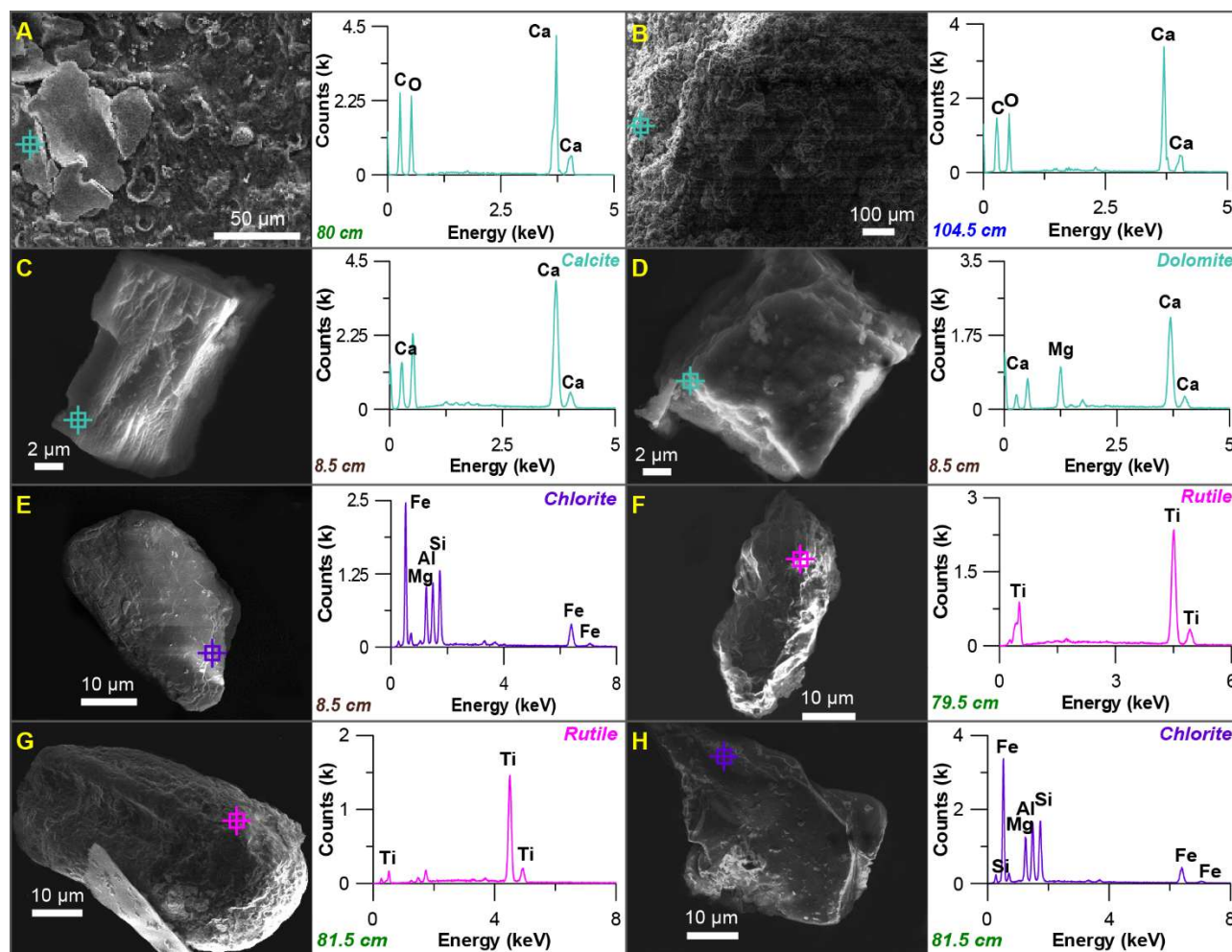
1206



1207

1208 **Figure 4. Ordination diagram.** The vectors (arrows) represent the confidence scores of
 1209 selected variables on principal components (PCs) 1 and 2, which together account for most of
 1210 the explanatory power. Samples were colour-coded according to the unit classification shown
 1211 in Figs. 2-3, while proxies were colour-coded as in Fig. 3B-C. Factor loadings for PCs 1 and 2
 1212 are presented in Table S1.

1213



1214

1215 **Figure 5. SEM images and SEM-EDS spectra of authigenic carbonates, and**1216 **representative clastic carbonate and Fe-Ti-rich material. A-B.** Authigenic Ca carbonates1217 from subunits 2a and 3a (80 and 104.5 cm, respectively). **C-D.** Detrital <20 μm carbonate clasts1218 (calcite and dolomite) from subunit 1a (8.5 cm) within the EM 2 modal range. **E-H.** Detrital

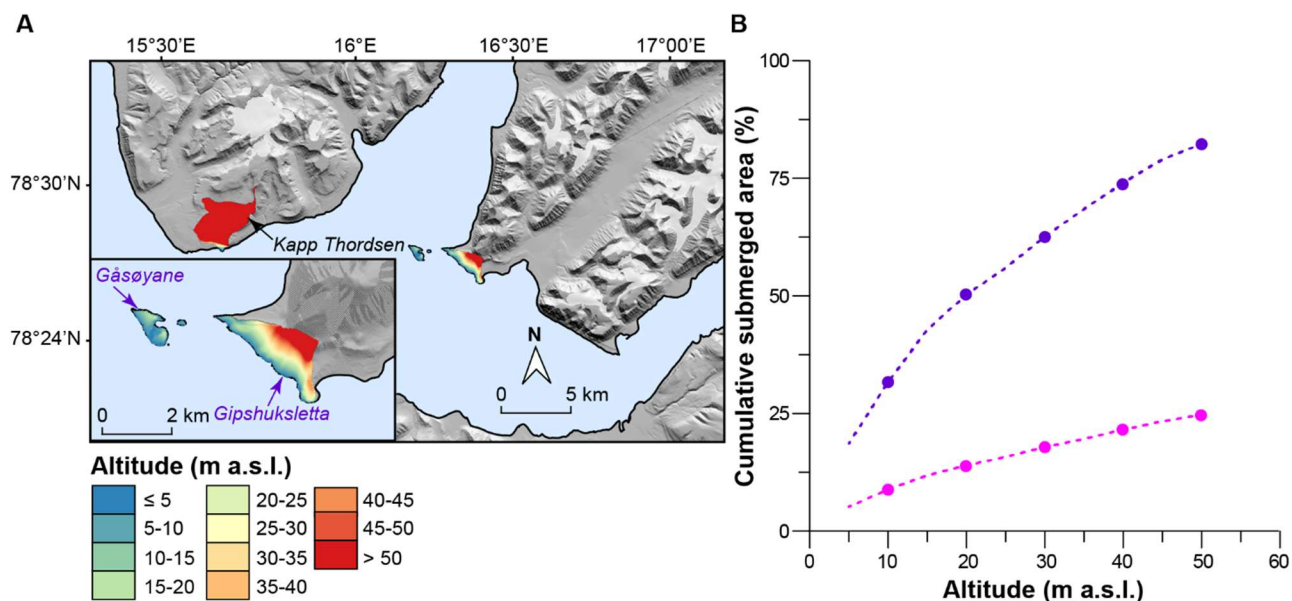
1219 >20 μm Fe-Ti-rich clasts (presumably chlorite and rutile) from subunit 1a (8.5 cm) and unit 2

1220 (79.5 and 81.5 cm) within EM 3 modal grain-size range. Crosshairs indicate EDS analysis spots,

1221 while adjacent spectra correspond to the marked locations. SEM-EDS elemental or oxide

1222 compositions and the interpreted mineralogy are listed in Tables S2-S3. Colour-coding follows

1223 the proxy colouring presented in Figs. 3B and 4.



1224

1225 **Figure 6. ArcticDEM 2 m mosaic-derived altitude and cumulative hypsometry of mapped**1226 **dolerite outcrop areas** (NPI Geological maps, 2026; Porter et al., 2023). **A.** Map of the studied

1227 dolerite outcrops in Kapp Thordsen, Gåsøyane and Gipshuksletta, coloured by altitude classes

1228 (m a.s.l.; Porter et al., 2023). **B.** Cumulative submerged area expressed as % of dolerite outcrop

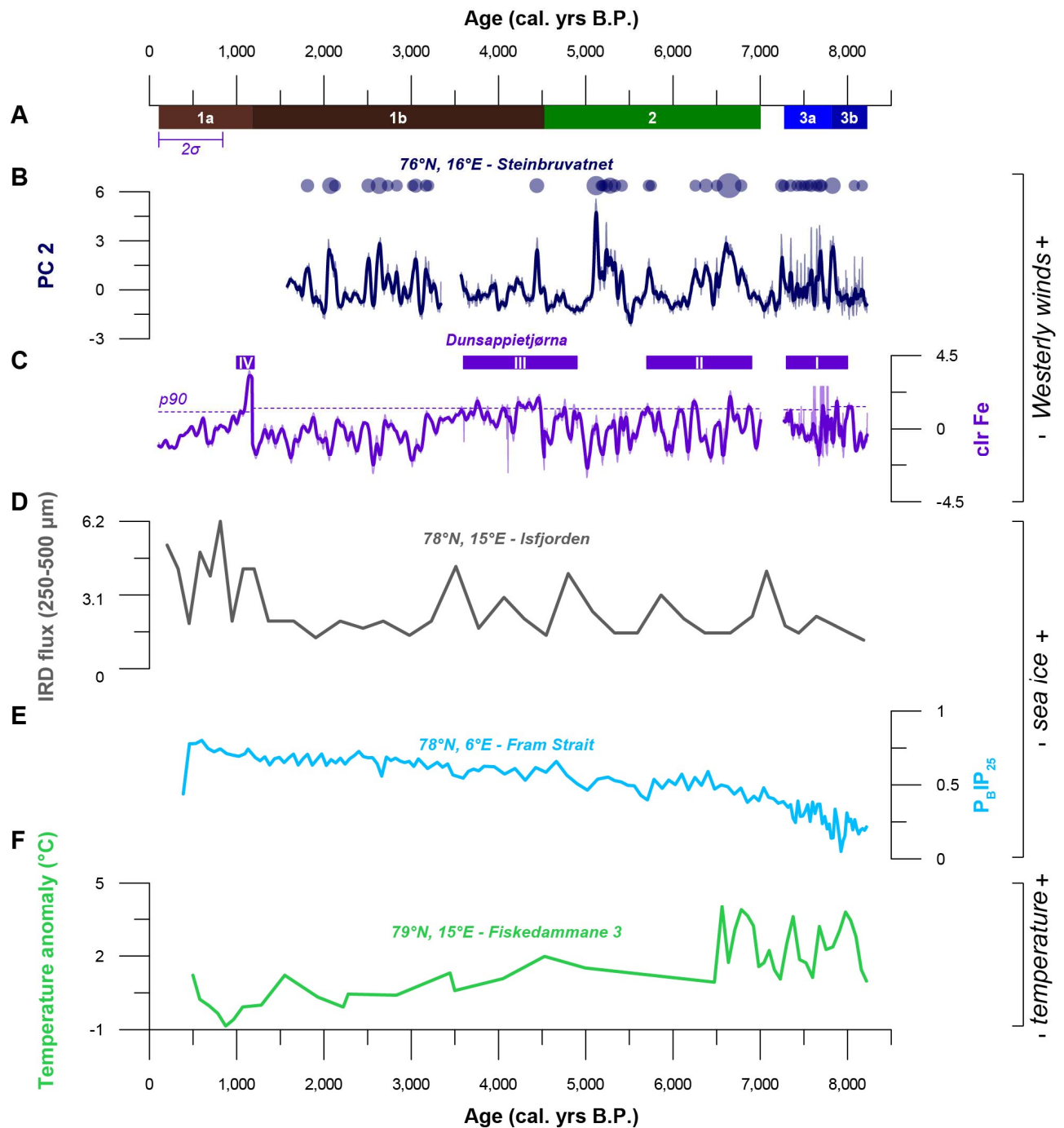
1229 area at or below a given altitude. The curves show the % of area that would be submerged if

1230 RSL reached that altitude (see also Fig. 2C), with the purple curve showing Gåsøyane and

1231 Gipshuksletta, and the magenta curve showing the combined area including Kapp Thordsen

1232 (see also Table S5; Porter et al., 2023).

1233



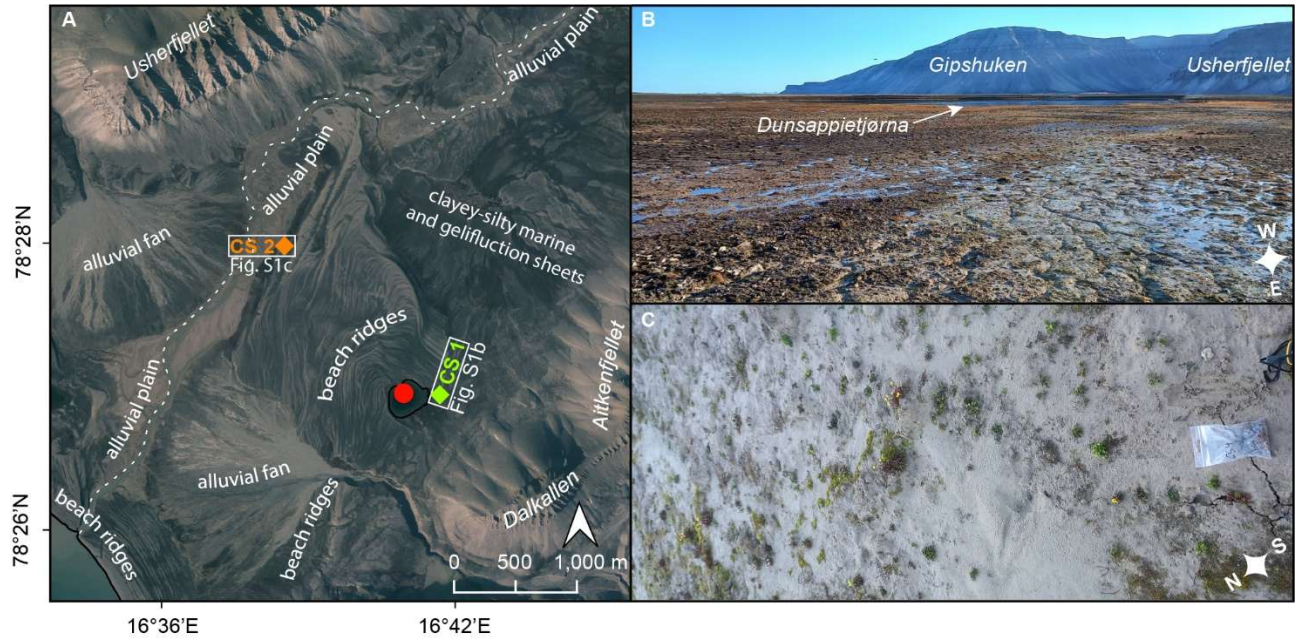
1234

1235 **Figure 7. Comparison of our clr Fe-derived Mid- and Late Holocene Westerly wind**
 1236 **reconstruction from Dunsappietjørna with relevant paleorecords from Svalbard and**
 1237 **Fram Strait.** Colour coding matches that presented in Fig. 1A-B, where we also map site
 1238 locations. **A.** Lithostratigraphic unit-subunit classification of the Dunsappietjørna record. The
 1239 purple horizontal bar marks the average calibrated 2σ age uncertainty of the record based on
 1240 the age-depth model presented in Fig. 2a. **B.** PC 2-based Westerly wind reconstruction from

1241 Steinbruvatnet, Southern Svalbard, with 30-year averages in bold and PC-2 derived Storm
1242 Magnitude Index (SMI) values calculated for maxima in Westerly winds, and shown as scaled
1243 circles (Stachowska et al., 2024). **C.** Clr Fe-based Westerly wind reconstruction from
1244 Dunsappietjørna, Central Spitsbergen, Svalbard (purple), standardised per units or subunits
1245 (Toonen et al., 2015), with 30-year averages in bold. Wind maxima are identified using a 90th
1246 percentile (*p90*) threshold (Hobday et al., 2016; Perkins-Kirkpatrick and Lewis, 2020), applied
1247 within each unit or subunit (see Fig. S8 for more details). Four major phases of the Mid- and
1248 Late Holocene Westerly maxima are marked by purple rectangles above the clr Fe curve and
1249 labelled with white Roman numerals. **D.** Central Isfjorden ice-rafted debris (IRD) record,
1250 plotted as IRD flux in the 250-500 μm size fraction from core JM98-845-PC (Rasmussen et al.,
1251 2012). **E.** Sea-ice cover data from Fram Strait (light blue), based on $\text{P}_{\text{BIP}25}$ (Müller et al., 2012a,
1252 b). **F.** Spring temperature reconstruction from the closed Fiskedammane 3 – a lake in Northern
1253 Spitsbergen (green), based on U_{37}^K (Kong et al., 2025).

1 Supplementary Information

2



3

4 **Figure S1. Catchment geomorphology and sedimentology of the Southern Gipsdalen. A.**

5 Aerial imagery of the study area, highlighting key geomorphic and sedimentary features (NPI

6 Map Data and Services, 2025). The locations of the studied sediment core DST-2023 GC (red

7 dot), the river – Gipsdalselva (dashed white line), and catchment samples (CSs) 1-2 (green and

8 light blue, respectively). **B.** Field photograph from the CS 1 location, showing ephemeral

9 streams flowing through the clayey-silty ground, Northeast of Dunsappietjørna. The lake basin,

10 Gipshuken and Usherfjellet are visible in the background. **C.** Field photograph from the CS 2

11 location, showing sedimentary deposits and tundra vegetation in the alluvial plain of the

12 Gipsdalselva, Northwest of the lake.

13



14

15 **Figure S2. Sentinel-2 satellite imagery (July 2023) showing peak dust accumulation in the**
 16 **area (ESA, EC, 2023). The study site is marked with a red dot.**

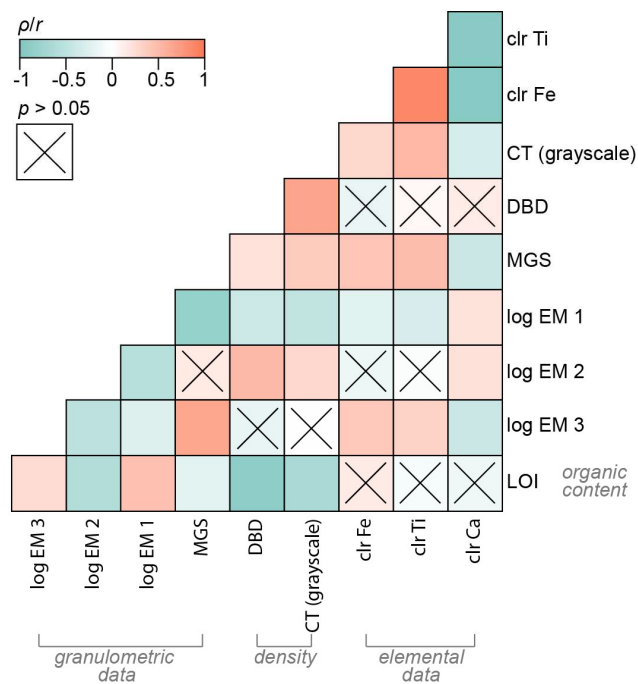
17

18 **Supplementary Note 1: Wind data from the Gåsøyane lighthouse station (2023-2024)**

19

20 Winter (DJF) is characterised by valley-induced North and Northeasterly winds, which prevail
 21 29% of the time with an average speed of 9.9 m/s (fresh breeze). While significant, the
 22 Easterlies are weaker, occurring 22% of the time at an average speed of 8.5 m/s (approximately
 23 a fresh breeze). Westerly winds are rare but occasionally the strongest, accounting for 8% of
 24 winter observations, with a mean speed of 12.3 m/s (strong breeze). On the contrary, Westerlies
 25 dominate in the summer (JJA), prevailing 45% of the time, though they are weaker, averaging
 26 5.3 m/s (gentle breeze). Winds descending from the valley's North maintain their strength and
 27 influence, occurring 21% of the time at an average speed of 7.0 m/s (moderate breeze), making
 28 them the most powerful summer system. Additionally, Southeasterlies occur 23% of the time
 29 at 5.8 m/s (moderate breeze; Frank et al., 2023).

30



31

32 **Figure S3. Proxy correlations.** We calculated Spearman's rank correlation coefficients (ρ) for
 33 all proxy pairs, except for comparisons between physical measurements and resampled
 34 scanning data, for which we applied cross-correlation (r ; see 'Methods' and Table 2 in the main
 35 manuscript). Crossed-out boxes indicate results with $p > 0.05$. The graph was prepared in ChiPlot
 36 (ChiPlot, 2023).

37

38 **Supplementary Note 2: Authigenic carbonates in Dunsappietjørna sediments**

39

40 In-lake carbonate precipitation typically occurs during whiting events, most pronounced in
 41 summer, when rising water temperatures reduce calcite solubility, thereby promoting
 42 precipitation. The extent of this process is influenced by multiple factors, including seasonal
 43 hydrology, water pH and hardness, phytoplankton blooms, and primary productivity (Boyall et
 44 al., 2023; K uchler-Krischun and Kleiner, 1990; Mazurek et al., 2012; Ohlendorf and Sturm,
 45 2001; Vanderploeg et al., 1987). Unlike in spring, when medium- to coarse-grained calcite
 46 precipitates, summer precipitation is dominated by smaller endogenic particles because the

47 formation of larger crystals is primarily driven by longer growth durations (Boyall et al., 2023;
48 K uchler-Krischun and Kleiner, 1990).

49

50 The presence of flake-like, anhedral authigenic carbonates (~10-50 μm ; see Fig. 5A-B in the
51 main manuscript) suggests that carbonate is preserved in a partially different form, compared
52 to the intact crystals or other forms described in (Boyall et al., 2023; K uchler-Krischun and
53 Kleiner, 1990; Mazurek et al., 2012; Vanderploeg et al., 1987). However, unlike in other
54 hardwater cold lake studies by Ohlendorf and Sturm (2001), where prolonged exposure to
55 undersaturated bottom waters during the ice-cover season results in complete calcite
56 dissolution, conditions in Dunsappietj orna favour partial preservation. Although we lack
57 sediment-trap data and direct observations, the conservation of authigenic carbonates is likely
58 due to high precipitation rates, as shown by sections with the highest authigenic carbonate
59 content, which coincide with peak sediment accumulation rates (SARs; see also Fig. 2B in the
60 main manuscript). In lakes with high calcite fluxes (>60% sediment calcite content), rapid
61 burial prevents calcite from dissolving (Lotter et al., 1997).

62

63 Additionally, we want to emphasise that the possibility of biologically induced calcite
64 precipitation cannot be ruled out, as the ice-free period coincides with peak lake temperatures
65 and potential phytoplankton blooms. Algal activity can promote the formation of ~30 μm
66 calcite crystals at water temperatures as low as +4°C, likely due to photosynthetic CO₂ uptake
67 by plankton in late summer (Ohlendorf and Sturm, 2001). During March 2024 fieldwork, we
68 observed a dense algal mat on the sediment surface, likely a remnant of the last bloom (see also
69 the '4.1. Core chronology' in the main manuscript).

70

Variable	PC 1	PC 2
DBD	0.11	0.47
LOI	-0.12	-0.51
log EM 1	-0.28	-0.25
log EM 2	-0.02	0.40
log EM 3	0.23	-0.26
CT (grayscale)	0.35	0.37
clr Ca	-0.48	0.21
clr Ti	0.51	-0.08
clr Fe	0.48	-0.21

71 **Table S1. Principal Component Analysis factor loadings.** Data shown for the two most
72 significant (71.47%) Principal Components (PCs) 1 and 2. For more details, see our ‘Methods’,
73 as well as ‘Results and Discussion’ sections in the main manuscript.

74

Fig. 5 panel	Depth (cm)	C	O	Mg	Al	Si	S	Ca
A	80	10.64	45.16	0.00	0.00	0.26	0.00	43.66
B	104.5	9.99	42.13	0.29	0.34	0.54	0.61	46.09

75 **Table S2. SEM-EDS elemental compositions (wt%) of authigenic carbonates.** Each entry
76 corresponds to an SEM-EDS spectrum shown in Fig. 5A-B (see the main manuscript).

77

Figure and panel	Depth (cm) or source	Na ₂ O	MgO	Al ₂ O ₃	SiO ₂	P ₂ O ₅	K ₂ O	CaO	TiO ₂	MnO	Fe ₂ O ₃	Interpreted mineralogy
5C	8.5	0.10	1.23	0.85	1.32	0.00	0.00	95.40	0.47	0.24	0.35	calcite
5D	8.5	0.22	28.96	3.51	6.87	0.21	0.24	58.67	0.00	0.07	1.13	dolomite
5E	8.5	1.65	15.16	16.84	26.29	0.08	1.09	1.21	0.13	0.63	36.94	chlorite
5F	81.5	0.00	0.28	0.38	1.17	0.00	0.01	0.22	97.23	0.00	0.71	rutile
5G	81.5	0.00	0.50	1.24	3.59	0.03	0.42	0.95	92.93	0.00	0.33	rutile
5H	81.5	0.26	14.78	21.20	28.31	0.00	0.57	1.15	0.16	0.28	33.28	chlorite
S6A	CS 1	0.22	11.16	1.61	4.70	0.00	0.27	79.62	0.16	0.15	1.91	dolomite
S6B	CS 1	0.36	15.17	1.03	3.10	0.00	0.20	79.02	0.26	0.00	0.29	dolomite

79 **Table S3. SEM-EDS oxide compositions (wt%) of detrital carbonate grains and Fe-Ti-rich, dolerite-derived clasts, together with**

80 **interpreted mineral phases.** Oxide data were normalised to 100 wt% prior to mineral identification. Each row reports a representative spectrum

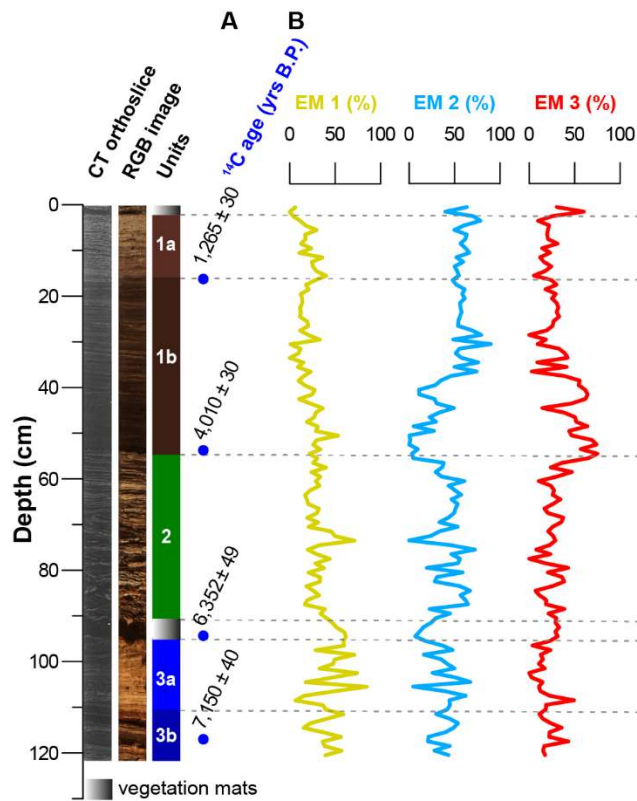
81 for the grains shown in Figs. 5C-H and S6A-B, as multiple spectra (typically n=5 or 6) were acquired per grain to assess its oxide composition.

Depth (cm) or source	Na ₂ O	MgO	Al ₂ O ₃	SiO ₂	P ₂ O ₅	K ₂ O	CaO	TiO ₂	MnO	Fe ₂ O ₃	Interpreted mineralogy
79.5	1.03	15.92	24.92	33.25	0.22	1.82	0.46	0.22	0.00	22.16	Fe-rich mica or chlorite
79.5	1.00	8.38	18.75	48.74	0.79	4.75	9.40	0.03	0.10	8.05	hornblende or Ca-rich plagioclase
81.5	1.98	14.56	24.70	50.33	0.31	2.04	4.17	1.77	0.00	0.13	altered chlorite
81.5	0.28	6.62	16.98	37.58	0.13	8.57	0.83	3.41	0.95	24.64	biotite
CS 2	0.82	13.18	19.28	43.31	0.19	3.79	1.11	0.30	0.08	17.94	biotite
CS 2	1.00	15.21	14.80	38.57	0.41	3.43	6.53	0.37	0.13	19.55	biotite

82 **Table S4. Additional SEM-EDS oxide compositions (wt%) of Fe-Ti-rich, dolerite-derived clasts, together with interpreted mineral phases, provided for completeness and not illustrated in Fig. 5.** Oxide data were normalised to 100 wt% prior to mineral identification. Each row reports

84 a representative spectrum, as multiple spectra (typically $n=5$ or 6) were acquired per grain to assess its oxide composition.

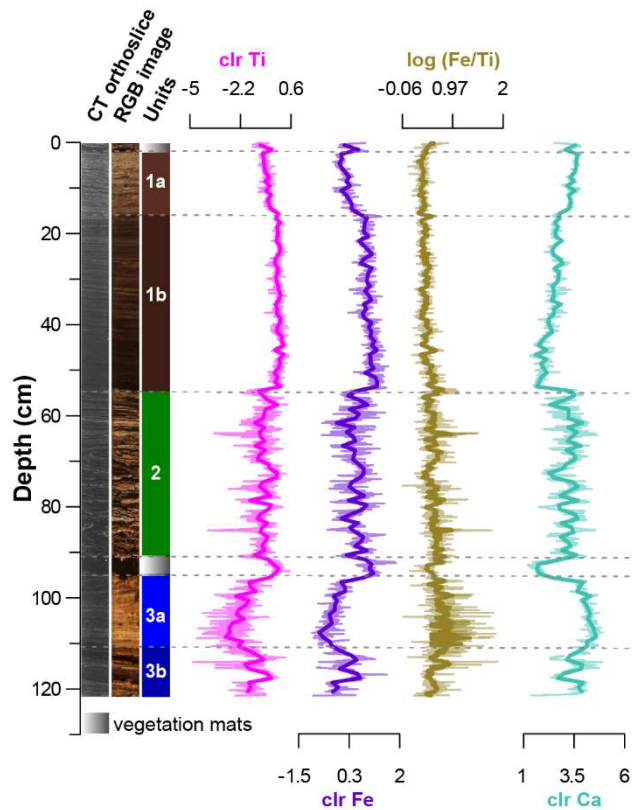
85



87

88 **Figure S4. End-Member Modelling Analysis (EMMA) results (Dietze et al., 2022; Prins**
 89 **and Weltje, 1999).** From the left: CT and optical imagery, and (sub)units classification of the
 90 sedimentary record. **A.** Position of ^{14}C samples with ^{14}C ages \pm errors (yrs). **B.** Downcore
 91 variability in EMs abundances (%; Prins and Weltje, 1999). Colour-coding for EMs follows the
 92 proxy colouring shown in Figs. 3B-C and 4 of the main manuscript.

93



94

95 **Figure S5. Key proxies for detrital input and variations in the non-detrital Fe measured**

96 **in Dunsappietjørna sediments.** From the left: CT orthoslice and RGB image with

97 lithostratigraphic units; centred log-ratios (clr) of Ti and Fe as proxies for minerogenic input

98 (Auer et al., 2025; Bertrand et al., 2024; Davies et al., 2015; Stachowska et al., 2024); log(Fe/Ti)

99 ratio, isolating the non-detrital Fe component (Blanchet et al., 2009; Davies et al., 2015); and

100 clr calcium (Ca) as a proxy for carbonates (Davies et al., 2015). Elevated log(Fe/Ti) values

101 indicate intervals where Fe variability is likely influenced by processes other than clastic input,

102 e.g., redox-related processes (Blanchet et al., 2009; Davies et al., 2015; Kylander et al., 2011),

103 while negative or stable values suggest dominance of detrital Fe co-varying with Ti (see also

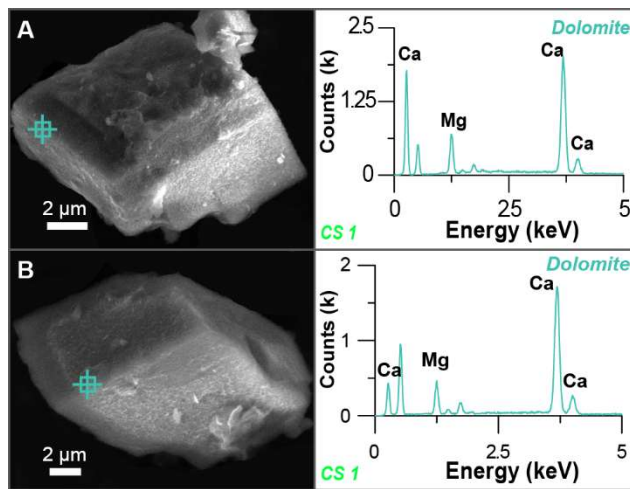
104 ‘The Mid- to Late Holocene evolution of Dunsappietjørna’ in the main manuscript). Colour-

105 coding for clr Ti, Fe and Ca follows the proxy colouring shown in Figs. 3B, 4 and 5 of the main

106 manuscript.

107

108



109

110 **Figure S6. SEM images and SEM-EDS spectra of carbonate clasts identified in CS 1 (A-**
111 **B).** Crosshairs indicate EDS analysis spots, while adjacent spectra correspond to the marked
112 locations. SEM-EDS elemental compositions and the interpreted mineralogy are listed in Table
113 S3. Colour-coding follows the proxy colouring presented in Figs. 3B and 4 of the main
114 manuscript.

115

Altitude (m a.s.l.)	G-G area (m ²)	G-G-K. T. area (m ²)	G-G total %	G-G-K. T. total %	G-G cumulative %	G-G-K. T. cumulative %
0-5	650735	691274	18.59	5.17	18.59	5.17
5-10	458720	487525	13.1	3.65	31.69	8.82
10-15	389376	405382	11.12	3.03	42.81	11.85
15-20	260296	280568	7.43	2.1	50.24	13.95
20-25	200563	244306	5.73	1.83	55.97	15.78
25-30	231492	270969	6.61	2.03	62.58	17.81
30-35	205885	240029	5.88	1.8	68.46	19.6
35-40	194158	261379	5.55	1.96	74.01	21.56
40-45	174951	237904	5	1.78	79.01	23.34
45-50	114152	177105	3.26	1.33	82.27	24.66

116 **Table S5. Hypsometric area distribution of mapped dolerite outcrops derived from the 2 m ArcticDEM mosaic (Porter et al., 2023).** Outcrop

117 area (m²) is reported for 5 m altitude bins (m a.s.l.) for two spatial extents: G-G (Gåsøyane and Gipshuksletta) and G-G-K. T. (Gåsøyane and

118 Gipshuksletta combined with Kapp Thordsen; see Fig. 6A-B in the main manuscript). 'Total %' shows the proportion of the total outcrop area

119 falling within each altitude bin, while 'cumulative %' gives the proportion of outcrop area lying at or below each altitude bin upper limit,

120 corresponding to the fraction that would be submerged if relative sea-level (RSL) reached that altitude (see also Fig. 2C in the main manuscript).

121 **Supplementary Note 3: Mid- and Late Holocene evolution of dolerite source availability**
122 **under relative sea-level change and implications for signal stability**

123

124 The gradual stabilisation of the Fe-Ti-rich dolerite-derived signal throughout the DST-2023-
125 GC record is unlikely to reflect wind variability alone, but also changes in source-area
126 availability linked to glacio-isostatic uplift and relative sea-level (RSL) fall, as discussed in
127 section 4.3 and illustrated in Figs. 3C and 6A-B of the main manuscript. Importantly, we do not
128 geochemically fingerprint the dolerite-derived fraction to a specific outcrop, and therefore treat
129 the mapped outcrops as a combined set of source areas.

130

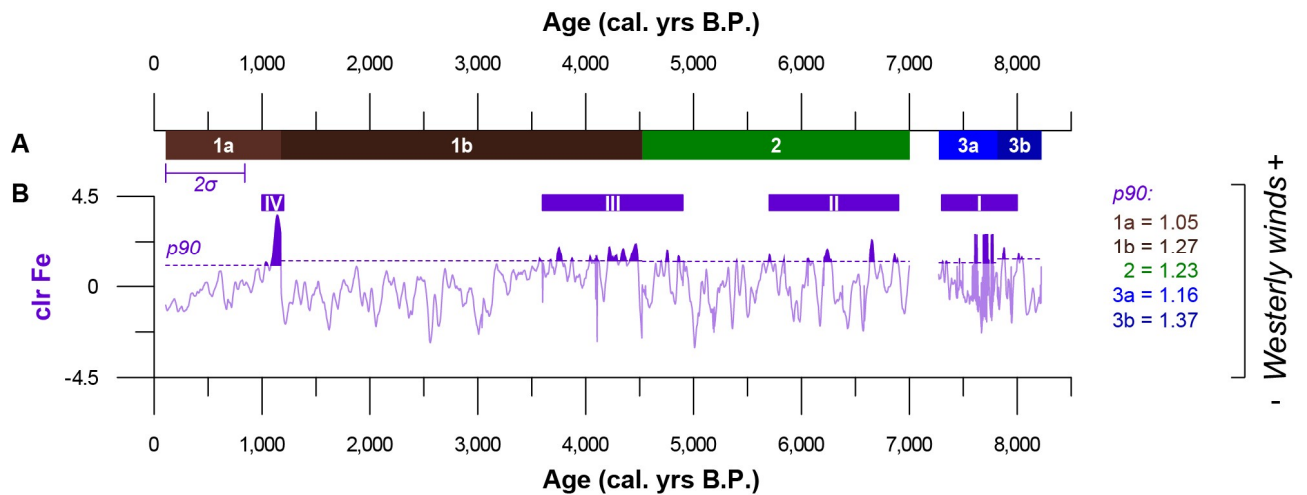
131 Within that framework, the local RSL curve (Fig. 2C) implies that at the onset of the DST-
132 2023-GC record (Strzelecki et al., 2026), a substantial % of the nearest, low-lying dolerite
133 outcrop area on Gåsøyane and Gipshuksletta would have been submerged (purple curve in Fig.
134 6B), reducing the subaerial area available for deflation and entrainment of dolerite-derived
135 material. This might help to contextualise the comparatively weaker Fe-Ti-rich input in unit 3
136 compared to the rest of the record (see 4.2.2 of the main manuscript), even under favourable
137 Westerly winds. As emergence progressed through the Mid- and Late Holocene, the % of
138 submerged outcrop area dropped, favouring more persistent dolerite-derived input. When the
139 higher-altitude Kapp Thordsen outcrops are included (Fig. 6A and magenta curve in 6B), the
140 cumulative submerged area remains much lower across the same altitude range, indicating that
141 a broader, mixed source domain would have been less sensitive to early RSL.

142

143 We also note that if low-lying outcrops dominated the dolerite signal, it should be most sensitive
144 to RSL-driven exposure changes. In contrast, a substantial contribution from higher-altitude

145 outcrops would likely dampen that sensitivity. These hypsometry-based constraints therefore
 146 support interpreting the Mid- and Late Holocene signal enhancement as partly a source-
 147 availability effect, without addressing site-specific provenance.

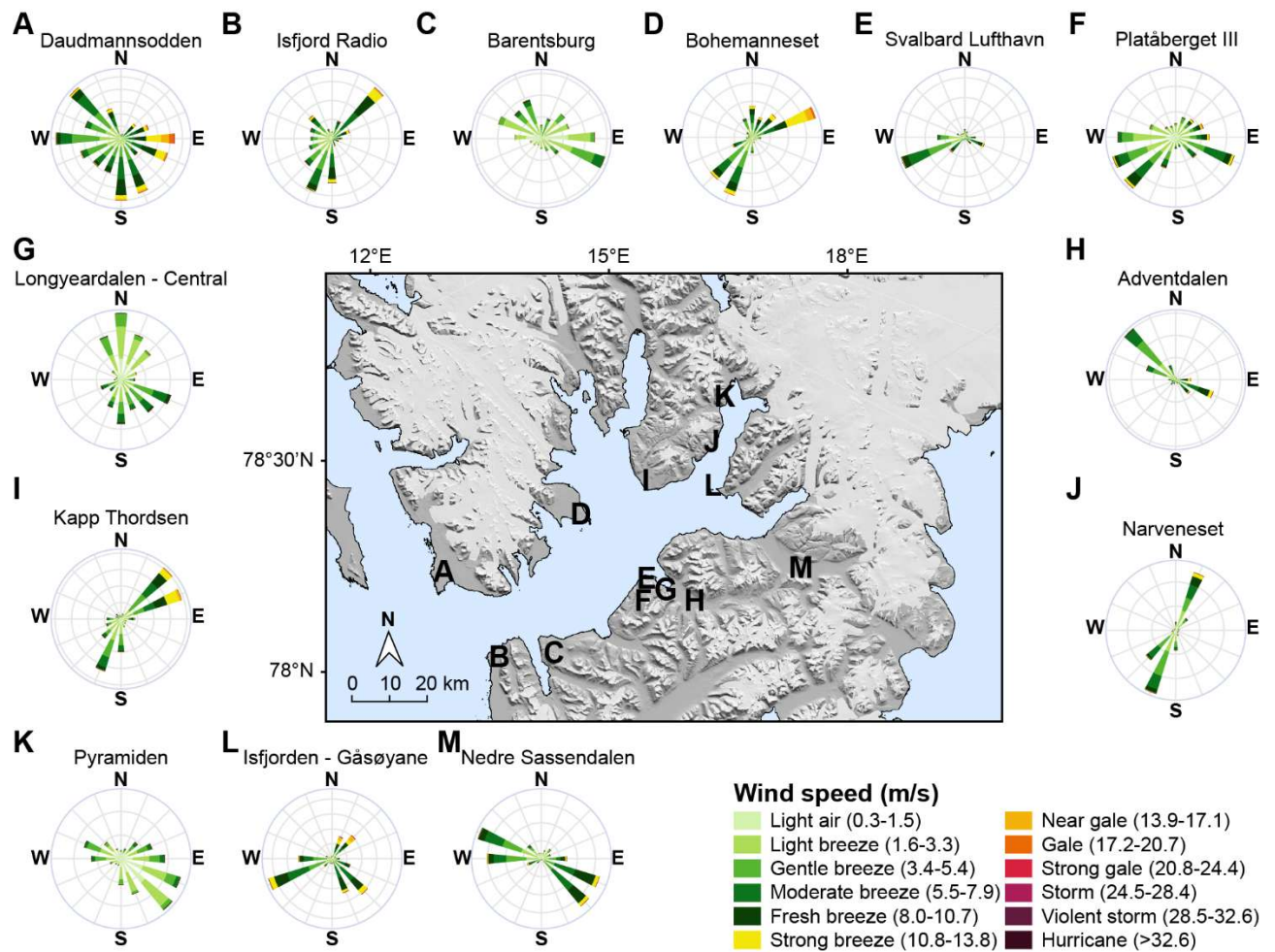
148



149

150 **Figure S7. Clr Fe-derived Mid- and Late Holocene Westerly wind reconstruction from**
 151 **Dunsappietjørna sediments, Central Spitsbergen, Svalbard. A.** Lithostratigraphic unit-
 152 subunit classification of the record. The purple horizontal bar indicates the average calibrated
 153 2σ age uncertainty for the record, based on the age-depth model shown in Fig. 2A of the main
 154 manuscript. **B.** Clr Fe-based Westerly wind reconstruction from the record, standardised per
 155 units or subunits (Toonen et al., 2015), with 30-year averages in bold. Wind maxima are
 156 identified using a 90th percentile (*p90*) threshold (Hobday et al., 2016; Perkins-Kirkpatrick and
 157 Lewis, 2020), applied within each unit or subunit. Four major phases of the Mid- and Late
 158 Holocene Westerly maxima are marked by purple rectangles above the clr Fe curve and labelled
 159 with white Roman numerals. Colour-coding for clr Fe follows the proxy colouring shown in
 160 Figs. 3B, 4, 5E, H and 7C of the main manuscript.

161



162

163 **Figure S8. June-August (JJA) wind roses and wind speed data (m/s) from 13 weather**
 164 **stations located in Isfjorden (in the centre).** Data for recurring JJA periods between 2015 and
 165 2025 (MET Norway, 2026). **A.** Daudmannsodden (2025). **B.** Isfjord Radio (2015-2025). **C.**
 166 Barenstburg (2015-2016). **D.** Bohemanneset (2025). **E.** Svalbard Lufthavn (2015-2025). **F.**
 167 Platåberget III (2018-2025). **G.** Longyeardalen – Central (2024-2025). **H.** Adventdalen (2017-
 168 2025). **I.** Kapp Thordsen (2025). **J.** Narveneset (2025). **K.** Pyramiden (2015-2023). **L.** Isfjorden
 169 – Gåsøyane (2025). **M.** Nedre Sassendalen (2021-2025).

170

171 References

172 NPI Map Data and Services: <https://geodata.npolar.no/>, last access: 10 April 2025.

173 ESA, EC: <https://apps.sentinel-hub.com/eo-browser/>, last access: 26 November 2023.

- 174 ChiPlot: <https://www.chiplot.online/>, last access: 18 August 2023.
- 175 Auer, A. G., Van Der Bilt, W. G. M., Schomacker, A., Bakke, J., Støren, E. W. N., Buckby, J.
176 M., Cederstrøm, J. M., and Van Der Plas, S.: Hydroclimate intensification likely aided glacier
177 survival on Svalbard in the Early Holocene, *Commun Earth Environ*, 6, 100,
178 <https://doi.org/10.1038/s43247-025-02064-z>, 2025.
- 179 Bertrand, S., Tjallingii, R., Kylander, M. E., Wilhelm, B., Roberts, S. J., Arnaud, F., Brown,
180 E., and Bindler, R.: Inorganic geochemistry of lake sediments: A review of analytical
181 techniques and guidelines for data interpretation, *Earth-Science Reviews*, 249, 104639,
182 <https://doi.org/10.1016/j.earscirev.2023.104639>, 2024.
- 183 Blanchet, C. L., Thouveny, N., and Vidal, L.: Formation and preservation of greigite (Fe₃ S₄)
184 in sediments from the Santa Barbara Basin: Implications for paleoenvironmental changes
185 during the past 35 ka, *Paleoceanography*, 24, 2008PA001719,
186 <https://doi.org/10.1029/2008PA001719>, 2009.
- 187 Boyall, L., Valcárcel, J. I., Harding, P., Hernández, A., and Martin-Puertas, C.: Disentangling
188 the environmental signals recorded in Holocene calcite varves based on modern lake
189 observations and annual sedimentary processes in Diss Mere, England, *J Paleolimnol*, 70, 39–
190 56, <https://doi.org/10.1007/s10933-023-00282-z>, 2023.
- 191 Davies, S. J., Lamb, H. F., and Roberts, S. J.: Micro-XRF Core Scanning in Palaeolimnology:
192 Recent Developments, in: *Micro-XRF Studies of Sediment Cores: Applications of a non-*
193 *destructive tool for the environmental sciences*, edited by: Croudace, I. W. and Rothwell, R.
194 G., Springer Netherlands, Dordrecht, 189–226, https://doi.org/10.1007/978-94-017-9849-5_7,
195 2015.
- 196 Dietze, M., Schulte, P., and Dietze, E.: Application of end-member modelling to grain-size
197 data: Constraints and limitations, *Sedimentology*, 69, 845–863,
198 <https://doi.org/10.1111/sed.12929>, 2022.
- 199 Hobday, A. J., Alexander, L. V., Perkins, S. E., Smale, D. A., Straub, S. C., Oliver, E. C. J.,
200 Benthuyssen, J. A., Burrows, M. T., Donat, M. G., Feng, M., Holbrook, N. J., Moore, P. J.,
201 Scannell, H. A., Sen Gupta, A., and Wernberg, T.: A hierarchical approach to defining marine
202 heatwaves, *Progress in Oceanography*, 141, 227–238,
203 <https://doi.org/10.1016/j.pocean.2015.12.014>, 2016.
- 204 Kuchler-Krischun, J. and Kleiner, J.: Heterogeneously nucleated calcite precipitation in Lake
205 Constance. A short time resolution study, *Aquatic Science*, 52, 176–197,
206 <https://doi.org/10.1007/BF00902379>, 1990.
- 207 Kylander, M. E., Ampel, L., Wohlfarth, B., and Veres, D.: High-resolution X-ray
208 fluorescence core scanning analysis of Les Echets (France) sedimentary sequence: new
209 insights from chemical proxies: XRF CORE SCANNING ANALYSIS OF LES ECHETS
210 SEDIMENTARY SEQUENCE, *J. Quaternary Sci.*, 26, 109–117,
211 <https://doi.org/10.1002/jqs.1438>, 2011.
- 212 Lotter, A. F., Sturm, M., Teranes, J. L., and Wehrli, B.: Varve formation since 1885 and high-
213 resolution varve analyses in hypertrophic Baldeggersee (Switzerland), *Aquatic Science*, 59,
214 304–325, <https://doi.org/10.1007/BF02522361>, 1997.

215 Mazurek, M., Paluszkiewicz, R., Rachlewicz, G., and Zwoliński, Z.: Variability of Water
216 Chemistry in Tundra Lakes, Petuniabukta Coast, Central Spitsbergen, Svalbard, The
217 Scientific World Journal, 2012, 1–13, <https://doi.org/10.1100/2012/596516>, 2012.

218 MET Norway: <https://seklima.met.no/>, last access: 2 January 2026.

219 Ohlendorf, C. and Sturm, M.: Precipitation and Dissolution of Calcite in a Swiss High Alpine
220 Lake, Arctic, Antarctic, and Alpine Research, 33, 410–417,
221 <https://doi.org/10.1080/15230430.2001.12003449>, 2001.

222 Perkins-Kirkpatrick, S. E. and Lewis, S. C.: Increasing trends in regional heatwaves, Nat
223 Commun, 11, 3357, <https://doi.org/10.1038/s41467-020-16970-7>, 2020.

224 Porter, C., Howat, I., Noh, M.-J., Husby, E., Khuvis, S., Danish, E., Tomko, K., Gardiner, J.,
225 Negrete, A., Yadav, B., Klassen, J., Kelleher, C., Cloutier, M., Bakker, J., Enos, J., Arnold,
226 G., Bauer, G., and Morin, P.: ArcticDEM - Mosaics, Version 4.1 (1.0),
227 <https://doi.org/10.7910/DVN/3VDC4W>, 2023.

228 Prins, M. A. and Weltje, G. J.: End-member modeling of siliciclastic grain-size distributions:
229 The late Quaternary record of aeolian and fluvial sediment supply to the Arabian Sea and its
230 paleoclimatic significance, in: Numerical experiments in stratigraphy: Recent advances in
231 stratigraphic and sedimentologic computer simulations, edited by: Harbaugh, J., Society for
232 Sedimentary Geology, 91–111, 1999.

233 Stachowska, Z., Van Der Bilt, W. G. M., and Strzelecki, M. C.: Coastal lake sediments from
234 Arctic Svalbard suggest colder summers are stormier, Nat Commun, 15, 9688,
235 <https://doi.org/10.1038/s41467-024-53875-1>, 2024.

236 Strzelecki, M. C., Lindhorst, S., Hein, C. J., van der Bilt, W. G. M., Kivimaki, K. E., and
237 Kavan, J.: 10,000 years of centennially-resolved climate and sea-level change archived in
238 Svalbard beach-ridge system, Sci Rep, <https://doi.org/10.1038/s41598-025-33652-w>, 2026.

239 Toonen, W. H. J., Winkels, T. G., Cohen, K. M., Prins, M. A., and Middelkoop, H.: Lower
240 Rhine historical flood magnitudes of the last 450years reproduced from grain-size
241 measurements of flood deposits using End Member Modelling, CATENA, 130, 69–81,
242 <https://doi.org/10.1016/j.catena.2014.12.004>, 2015.

243 Vanderploeg, H. A., Eadie, B. J., Liebig, J. R., Tarapchak, S. J., and Glover, R. M.:
244 Contribution of Calcite to the Particle-Size Spectrum of Lake Michigan Seston and Its
245 Interactions with the Plankton, Can. J. Fish. Aquat. Sci., 44, 1898–1914,
246 <https://doi.org/10.1139/f87-234>, 1987.

247